ANKARA YILDIRIM BEYAZIT UNIVERSITY

GRADUATE SCHOOL OF NATURAL AND APPLIED SCIENCES

DEVELOPMENT AND CHARACTERIZATION OF 3D-PRINTED FREQUENCY-SELECTIVE SURFACE STRUCTURES IN AEROSPACE APPLICATIONS

M.Sc. Thesis by

Ömer Ziyaeddin ALABOYUN

Department of Aerospace Engineering

February, 2023

ANKARA

DEVELOPMENT AND CHARACTERIZATION OF 3D-PRRINTED FREQUENCY-SELECTIVE SURFACE STRUCTURES IN AEROSPACE APPLICATIONS

A Thesis Submitted to

The Graduate School of Natural and Applied Sciences of

Ankara Yıldırım Beyazıt University

In Partial Fulfillment of the Requirements for the Degree of Master of Science in Aerospace Engineering, Department of Aerospace Engineering

by

Ömer Ziyaeddin ALABOYUN

February, 2023

ANKARA

M.Sc. THESIS EXAMINATION RESULT FORM

We have read the thesis entitled **"DEVELOPMENT AND CHARACTERIZATION OF 3D-PRINTED FREQUENCY-SELECTIVE SURFACE STRUCTURES IN AEROSPACE APPLICATIONS"** completed by **ÖMER ZİYAEDDİN ALABOYUN** under the supervision of **Asst. Prof. METE BAKIR** as the thesis supervisor and we certify that in our opinion it is fully adequate, in scope and quality, as a thesis for the degree of Master of Science.

Asst. Prof. Mete BAKIR

Thesis Advisor

Prof. Veli ÇELİK (AYBU)

Jury Member

Assoc. Prof. Ersin BAHÇECİ (ISTE)

Jury Member

Prof. Sadettin ORHAN

Director

Graduate School of Natural and Applied Sciences

ETHICAL DECLARATION

I hereby declare that, in this thesis which has been prepared in accordance with the Thesis Writing Manual of the Graduate School of Natural and Applied Sciences,

- All data, information, and documents are obtained in the framework of academic and ethical rules,
- All information, documents, and assessments are presented in accordance with scientific ethics and morals,
- All the materials that have been utilized are fully cited and referenced,
- No change has been made to the utilized materials,
- All the works presented are original,

and in any contrary case of the above statements, I accept to renounce all my legal rights.

Date: 17.02.2023 **Signature:……..**

Name & Surname: Ömer Ziyaeddin ALABOYUN

ACKNOWLEDGEMENTS

In the name of Allah (swt), the most gracious and the most merciful. Firstly, I would like to express my sincere gratitude to my thesis advisor, Asst. Prof. Mete BAKIR, for his guidance. I would also like to thank Assoc. Prof. Oğuzhan Akgöl that he guided me all along my thesis work, research, and writing the report and paved the way for me to thoroughly understand EM materials and complete EM analyses and tests needed for this thesis. His excellent knowledge & experience and valuable recommendations set up the milestones of this study. I would also like to thank all the staff of Turkish Aerospace Industries, Inc. for their support. And then, I would like to express my love to my beautiful daughter Iman Erva for being funny and distracting me along the way, yet also being patient in postponing her games with her "babiş". Lastly, I would also want to express my deepest gratitude to my beloved wife Zeynep for her lifelong support, help, encouragement, and prayers.

Special thanks to Abdullah Gözüm, M. Harun Yamaç, Sinan Gözüm, Çağrı Akdeniz, Adem Can Uşak, Münevver Eryılmaz, Ümit Aytar, İbrahim E. Tekin, Hakan Demiröz and Yavuz Selim Gözüm for their significant contribution to this study. Also, this study was completed in loving memory of my brother Omar Ali Khalil who is no longer with us, yet he still inspires me in every aspect of my life.

2022, 17 February **Ömer Ziyaeddin ALABOYUN**

DEVELOPMENT AND CHARACTERIZATION OF 3D-PRINTED FREQUENCY-SELECTIVE SURFACE STRUCTURES IN AEROSPACE APPLICATIONS

ABSTRACT

In aerospace applications, 3D-printed materials are not used extensively due to the small amount of recorded data/information in the material library. But it does have a great potential to be used more often in future aerospace projects. With the current progress of technology, additive manufacturing methods gain a lot of attention due to their time-efficient production and cost-effectiveness. The fastest and cheapest methods of additive manufacturing are 3D-printed polymers most commonly generated by Fused Deposition Modeling. Other common methods of 3D Printers are Stereolithographic Apparatus and Selective Laser Sintering.

The main goal of this study is to reduce Radar Cross-section caused by antenna structure using two separate approaches. The first approach is to use the combination of metamaterial and frequency-selective surface structures together on the antenna radome. In this way, the frequency-selective surface will provide band-pass filtering property allowing certain frequencies to pass while reflecting all the others. In addition, the metamaterial structure acts as an electromagnetic absorber so that some of the reflected signals are absorbed yielding a lower Radar Cross-section. The second approach deals with the replacement of the metallic ground plane of the antenna with a frequency-selective surface acting as a band-stop filter backed with electromagnetic absorber foam which also causes a reduced radar cross-section. Metamaterial and frequency-selective surfaces are all made from periodic structures and a dielectric substrate. In this study, 3D-printed materials were used as the substrate of these periodic structures and their performances in terms of reducing radar cross-section were compared.

Fused Deposition Modeling is chosen to fabricate most of the test specimens in this study. And also, with the Stereolithographic Apparatus method, some electromagnetic and tensile test specimens are fabricated. Only one type of photo-curable resin which is ANYCUBIC Basic Resin is used with Stereolithographic Apparatus 3D printing,

then electromagnetic and tensile test specimens are fabricated. With the Fused Deposition Modeling method, several types of 3D printer thermoplastic filaments are used, which are PLA (Polylactic acid), ULTEM9085-FR (PEI Polyetherimide flame retardant), PC (Polycarbonate), and NYLON6-FR (Polyamide6 flame retardant). After 3D printing of specimens with certain raster and also infill orientations, the mechanical strengths of these specimens are characterized by tensile tests. In addition to tensile tests, electromagnetic tests are also conducted upon the specimens that are manufactured with respect to relevant 3D printing materials with certain raster and infill orientations as multilayered frequency-selective surface (FSS) structures. Eventually, electromagnetic characterization of the manufactured substrates along with the metamaterial and frequency-selective surface designs are studied to obtain radar cross-section reduction.

Keywords: Frequency-selective Surfaces, Metamaterials, 3D-printed Materials, Reducing Radar Cross-section, Elastic Modulus, Tensile Strength.

HAVACILIK UYGULAMALARINDA 3B YAZILMIŞ FREKANS SEÇİCİ YÜZEY YAPILARININ GELİŞTİRİLMESİ VE KARAKTERİZASYONU

ÖZ

Malzeme kütüphanelerinde yeterli sayıda kayıtlı veri/bilgi olmamasından dolayı 3B baskılı malzemeler havacılık ve uzay uygulamalarında kullanılmamaktadır. Ancak, gelecekte yapılacak havacılık ve uzay projelerinde daha sık kullanılmalarına dair yüksek bir potansiyele sahip ürünlerdir. Hızlı ve düşük maliyetli üretimlerinden dolayı teknolojideki gelişimlerle beraber eklemeli imalat yöntemleri büyük dikkat çekmeye başlamıştır. En hızlı ve en ucuz eklemeli imalat yöntemleri Fused Deposition Modeling (FDM) ile genelde üretilen 3D-baskılı polimerlerdir. Diğer yaygın 3D Yazıcılar Stereolithographic Apparatus (SLA) ve Selective Laser Sintering (SLS)'dir.

Bu çalışmada ulaşılmak istenen başlıca hedef, 2 farklı yöntem ile antenden kaynaklanan Radar Kesit Alanının düşürülmesi. İlk yaklaşım, anten radomu üzerinde metamalzeme ve frekans seçici yüzey yapılarının kombinasyonunu birlikte kullanmaktır. Bu şekilde frekans seçici yüzey, diğerlerini yansıtırken belirli frekansların geçmesine izin veren bant geçiren filtreleme özelliği sağlayacaktır. Ek olarak, metamalzeme yapısı elektromanyetik bir soğurucu görevi görür, böylece yansıyan sinyallerin bir kısmı sönümlenir ve daha düşük Radar Kesiti elde edilir. İkinci yaklaşım, antenin metalik zemin düzleminin, aynı zamanda azaltılmış bir radar kesitine neden olan elektromanyetik soğuran bir köpükle desteklenen ve bir bant durdurma filtresi görevi gören frekans seçici bir yüzeyle değiştirilmesiyle ilgilidir. Metamalzeme ve frekans seçici yüzeylerin tümü periyodik yapılardan ve bir dielektrik substrattan yapılır. Bu çalışmada, bu periyodik yapıların substratı olarak 3D baskılı malzemeler kullanılmış ve radar kesitinin azaltılması açısından performansları karşılaştırılmıştır.

Bu çalışmada, elektromanyetik ve çekme test numunelerinin çoğunu üretmek için FDM seçilmiştir ve SLA yöntemi ile de elektromanyetik ve çekme test numuneleri üretilmiştir. 3 boyutlu parça üretimi için SLA yöntemi ile yalnızca bir tip reçine kullanılmıştır, bu ANYCUBIC temel reçinedir. FDM ile farklı farklı 3B yazıcı termoplastik filament türleri kullanılmaktadır, bunlar PLA (Polylactic Acid),

ULTEM9085 FR (PEI Polyertherimide alev geciktirici), PC (Polycarbonate) ve NYLON6-FR (Polyamide6 alev geciktirici)'dır. Farklı raster ve dolgu yönelimlerine sahip numunelerin 3B baskılarından sonra, bu numunelerin mekanik dayanımları karakterize edilmiştir. Çekme kuvveti üzerine çalışılmış ve mekanik testler gerçekleştirilmiştir. Mekanik testlere ek olarak, çok katmanlı frekans seçici yüzeyler (FSS) ve metamalzemeler (MTM) olarak ilgili raster ve dolgu yönelimlerine bağlı olarak üretilen numunelere elektromanyetik testler gerçekleştirildi. En son olarak belli bir seviye elektro manyetik soğurma ve radar kesit alanında düşüş elde edilmesi için, elektromanyetik karakterizasyon ve FSS geliştirilme çalışmaları gerçekleştirildi.

Anahtar Kelimeler: Frekans Seçici Yüzeyler (FSY), Meta Malzemeler, 3B Yazılmış Malzemeler, Radar Kesit Alanı (RKA), Çekme Dayanımı

CONTENTS

NOMENCLATURE

Roman Letter Symbols

A	Cross-sectional area, mm^2
F_{max}	Maximum force, N
L	Length, mm
ΔL	Extension, mm
F	Frequency, GHz
P	Load, N
w	Width, mm
T	Transmission, dB
k	Wave Number
t_s	Sample Thickness, mm
t_m	Metal Plate Thickness, mm

Greek Letter Symbols

σ_{axial}	Axial Tensile Stress, MPa
$\sigma_{ultimate}$	Ultimate Tensile Stress, MPa
ε	Strain in Mechanical
σ	Stress /Strength in Mechanical, MPa
σ	RCS Value in EM
ΔL	Extension, mm
ε_r	Relative Electrical permittivity in EM, dB
μ_r	Relative Magnetic permeability, dB
Γ	Reflection, dB
λ	Wavelength, m

Acronyms

FDM	Fused Deposition Modelling
SLA	Stereo Lithographic Apparatus
SLS	Selective Laser Sintering
ASTM	American Society for Testing and Materials
RF	Radio Frequency
EM	Electro-Magnetic
FSS	Frequency-selective Surfaces

RCS	Radar Cross-section
CSRR	Circular Split Ring Resonator
LMS	Large – Medium – Small Configuration
SML	Small – Medium – Large Configuration
UTS	Universal Testing System
PEI	Polyetherimide
PC	Polycarbonate
PLA	Polylactic acid
ULTEM9085FR	Flame Retardant HP Polyetherimide (PEI) Thermoplastic
NYLON6 FR	Polyamide 6 (PA6) Flame Retardant

LIST OF TABLES

LIST OF FIGURES

CHAPTER 1

INTRODUCTION

In aerospace applications, one of the main concerns is to be undetectable to enemy radar systems. The term “radar” actually is the short version of “radio detection and ranging”, which refers to a system that uses radio frequency energy that is projected and reflected to detect and locate objects, measure distance or elevation, navigate, homing, bombardment and other tasks [1]. Because radar technology has advanced significantly, the development of low observable / stealth technologies for avoiding radar systems has become extremely crucial [2]. In order to improve the low observability performance, the radar cross-section (RCS) area must be kept to a minimum level. The lower the RCS, the lower chances to get detected since the detectable distance is proportional to the radar cross-section [3].

With the developing technology, the use of 3D-printed materials increasing day by day from agriculture to aerospace applications. As a result of these new 3D printing technologies, many types of materials can be fabricated within the field of material science with different methods of 3D printing, such as Fused Deposition Modeling (FDM), Selective Laser Sintering (SLS), Stereo Lithographic Apparatus (SLA), and etc... Every single 3D-printed fabrication depends upon additive manufacturing processes. Models are being created with computer-aided design tools and produced these models by 3D printers.

There are numerous materials (filaments) used by 3D printers including ASA, Polycarbonate, Nylon 6, ABS, PLA, ULTEM 9085/1010, and so on. In recent years, 3D printing technology started to be used in material engineering as well due to its fast production and lower cost in various fields [4]. A promising study field is the use of 3D printers to manufacture MTM absorbers for electromagnetic applications, despite the fact that numerous approaches have been examined in diverse studies. 3D printing

can definitely be preferred and used including the design of metamaterials along with frequency-selective surfaces mentioned by S. Ghosh and S. Lim as in [5]. These types of structures are preferred to reduce Radar Cross-section (RCS) in Aerospace [6]. 3D printing allows layer-by-layer fabrication of structures from a computer-aided model. This technology enables parts to be created with difficult geometries. Fused deposition modeling (FDM) is the most popular and handy additive manufacturing method. It offers one of the most cost-efficient ways of 3D printing [7]. Solid objects are created by melting a polymer filament which is deposited through a nozzle tip one layer on top of another. In [8], a manufactured FSS when compared to the identical design that was fully metalized, the resonant frequency was dramatically reduced and the angle of incidence performance was improved by partially metalizing 3-D printed structures [9]. Electromagnetic band gap (EBG) structures have been utilized frequently to enhance the performance of antenna [10]-[12]. For more efficient antenna in terms of matching and directivity, they can serve as high-impedance surfaces. There have been suggestions for small coplanar waveguide (CPW) antennas that use commercial laminates [10] and textile materials [11].

Detectability is often measured as RCS which is desired to be low in order to have low detectability property. Using different geometries and electromagnetic absorber materials on the surface of a vehicle is the basic option preferred. On the other hand, there are some places in which absorbing materials cannot be applied such as antennas and their cavities. Antennas are a crucial part of communication and radar in the aerospace industry and are made by reflecting materials yielding high RCS. Antennas are used with radomes which have to be transmitted materials so that the electromagnetic signal leaving or receiving the antenna is not distorted. The other significant problem is that antenna performances are distorted by electromagnetic waves caused by other sources and other antennas. Incoming EM signals may also harm the electronic parts of the air vehicles. Since we cannot eliminate antennas or their reflective materials, different approaches are needed to reduce the RCS caused by such antennas and also to minimize the distortion caused by EM waves coming from other sources.

In this study, we focus on two separate approaches. In the first one, we considered adding functional property on radome while in the second we dealt with the ground plane of the antennas in order to both reduce RCS caused by the antennas and minimize the EM distortion. Frequency-Selective Surfaces (FSS) were used as a band-pass filter on the radome which allows approximately full transmission at the operation frequency of the antenna while reflecting all other signals. Using band-pass filtering property on the radome will allow the radome to transmit or receive EM waves at a certain frequency band while reflecting all other signals minimizing the EM distortion on the operation of antennas. In addition, the metamaterial absorbing structure was designed at the back side of the FSS structure so that it does not affect the operation of the antenna while absorbing some EM signals at higher frequencies. In the second approach, we have placed an FSS structure with band-stop filtering property as the ground plane in order to have a full reflective ground plane at desired frequency bands. Besides, EM absorber foam was added under the FSS structure to absorb the electromagnetic waves at frequencies other than those used for band-stop filtering operation. In this way, the ground plane will be a full reflector at the desired frequencies while transmitting all other frequencies which will also be absorbed by the absorber foam placed at the back of the FSS ground plane.

Both MTM and FSS structures are manufactured on a dielectric material. In order to achieve our goal, 3D printing technology can be utilized due to its fast manufacturing, lightweight and low-cost. Band filtering (both band-pass and stop-band) FSS structures are designed and fabricated with 3D-printed dielectric materials as the substrate. The reason, that 3D printers were chosen, was to enable the capability of building difficult geometries such as the radome of antennas. The radome is a curved shape electromagnetic filtering and absorbing system that encapsulates radar antennas. And it provides a certain amount of RCS Reduction with FSS, Metamaterials, and a dielectric substrate in between.

1.1 Basics of 3D Printing

3D printing technology is very popular since the early 2000s. This technology allows any solid shape or geometry to be created with the digital manufacturing process of 3D Printing. The materials are added layer-by-layer in order to build 3D parts directly from the models that are generated with computer-aided design software. There are many advantages such as limitless design options no matter how complex the structure geometries are. And also, it brings the capability of low-cost and time-saving production. In 3D Printing, the most common methods, to create polymer-based components, are fused deposition modelling (FDM), selective laser sintering (SLS), and stereolithographic apparatus (SLA).

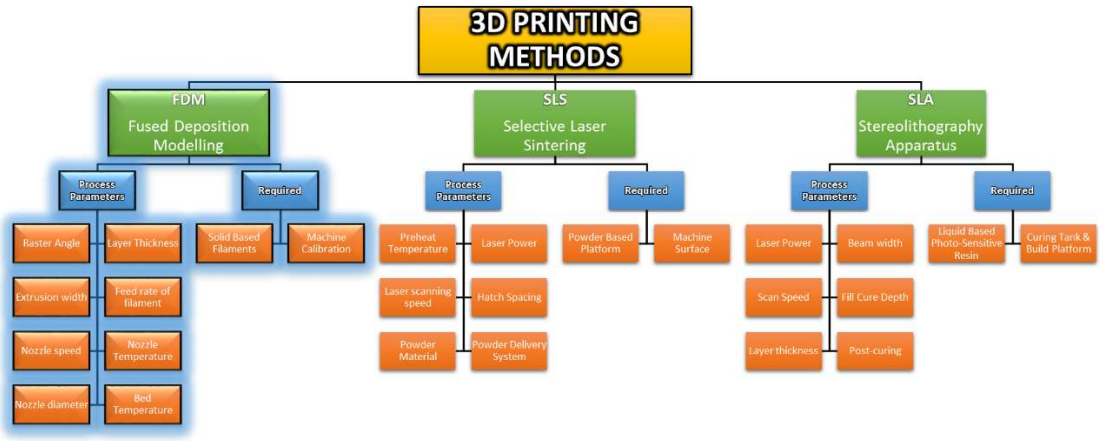

Figure 1.1 Polymer based 3D Printing Methods

In fused deposition modelling (FDM), 3D-printed part properties are affected by process parameters. These process parameters are raster angle, extrusion rate and width, temperature of bed (platform), temperature of nozzle and speed of nozzle. The angle between "nozzle's direction and one of the axes of the printing platform" is called the raster angle [16, 17].

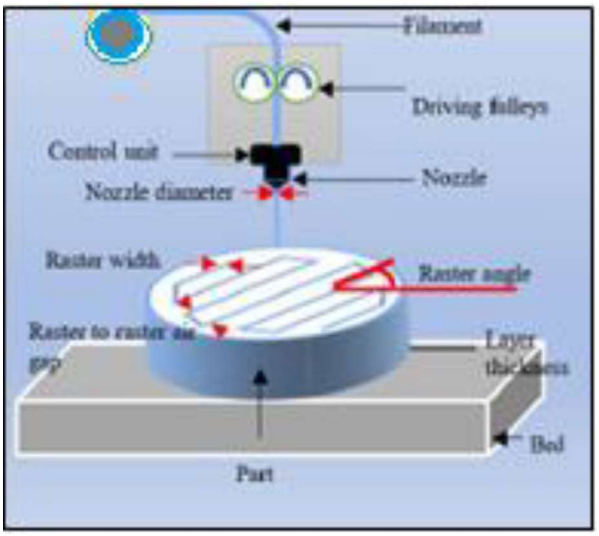

Figure 1.2 FDM Method ref. from [15]

The extrusion rate is the rate at the filament that is extruded from the tip of the nozzle onto the printing platform. The bed temperature is necessary to provide enough cohesion between the part being printed and the print platform to avoid warpages [18, 22]. The nozzle temperature is also essential since the filament is melted at the nozzle and it has a great influence on the structural/mechanical properties of 3D-printed objects [19].

Selective laser sintering (SLS) is another additive manufacturing 3D printing method that is widely used in the sector. This process is a variant of powder bed fusion. In an enclosed chamber, with the help of one or more laser beams, particles in powdered materials are selectively fused layer-by-layer in order to fabricate the product. The process is carried out up until the top layer of the product is fused. Upon completion of sintering, the unused is cleaned out from the extracted part within the printing platform. The most crucial parameter in SLS is the energy density which has a high influence on part property and the overall printing/sintering process [20].

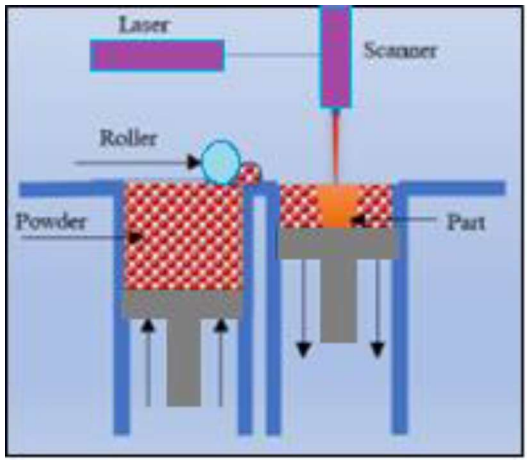

Figure 1.3 SLS Method ref. from [15]

In the Stereolithography apparatus (SLA), the photo-curable resin solidification, by using photo-polymerization, is initiated by absorbing the light. A pattern is laid out on the resin with the help of computer software. With the strikes of a laser beam on the resin, the resin gets hardened and a solid layer is obtained as it was patterned by the laser beam. And this principle is recurrently applied to the resin layer-by-layer. The light source energy and the time of exposure to laser light define the thickness of the layer [21]. There are three major process parameters that drastically effect the quality of the product with the SLA Printing method. These are fill-cure depth, thickness of layer, and post-curing process. Usually, in SLA, printed objects need a post-curing, and then this will improve the mechanical properties of the objects.

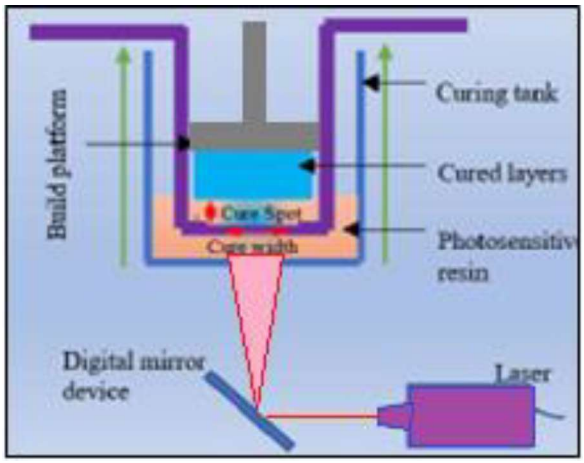

Figure 1.4 SLA Method ref. from [15]

In terms of time-saving production, cost-effective process, and simplicity in printing, the FDM is the most proper method for this study. Because the process is fast and as easy as heating up the plastic filament into a semi-liquid form and dispensing it on the 3D printing platform. It is also proven that a large number of material selections can be provided by FDM for 3D printing.

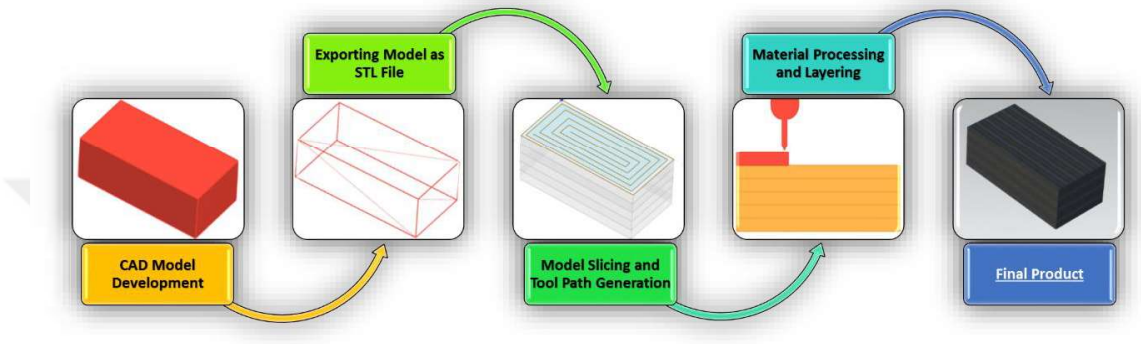

Figure 1.5 3D Printing Processes in five steps

1.2 Basics of FSS

FSS works as controlling the frequency bands that are needed for the absorption and transmission and reflection of electromagnetic waves. Frequency-selective surfaces (FSS) can be applied on a planar, curved, or multilayer surface. A conductive layer and dielectric material are the main components in order to design an FSS structure. The conductive layer can be fabricated by using copper rods, wires, conductive ink, or thin conductive strip lines used in most PCBs. Besides, the most common dielectric material is FR-4 because of its high efficiency and low-cost. In the related literature, most FSS studies are based on planar surfaces. On the other hand, numerous applications in the relevant industry require the application on curved or non-planar and even complex geometries. Radomes can be given as an example of such structures on which FSSs are expected to be applied. In antenna applications, it is desired to have radomes having band-pass or stop-band behaviors to improve isolation from other antennas or not to receive unwanted electromagnetic waves that can interfere with the

operation of the system. That is why, the use of FSS has significant role in the studies associated with antenna, and microwave engineering.

1.3 Basics of Radar Cross-section (RCS)

Radio detection and ranging, shortly known as radar, is composed of a system using radio frequency waves to detect the size and location of an object. RCS is the parameter that determines how much the object/target is visible or detectable by the radar. The higher the RCS, the larger the detectability of the object. In order to obtain low observability, RCS must be minimized since it is directly proportional to the detectable distance. The RCS depends upon different parameters, such as;

- The reflected angle of the incident EM wave
- The incident angle of the incident EM wave
- Polarization of the transmitted and received EM wave
- Material and size (relative and absolute) of the object

In conceptual terms, not all electromagnetic energy is directed to the target. Even though the distance and power of the radar are important for detecting objects, these are not the factors that are used in the RCS equation. The theoretical RCS (σ) can be characterized by reflectivity, directivity, and project cross-section. These are the variables required for computing RCS (σ). So that RCS depends mainly on the reflectivity of the targeted object. In terms of electromagnetics, the reflectivity can be defined as the percentage number of electromagnetic waves that scatter after being impacted on the target. For directivity, it can be said that some amount of the energy backscatters in the direction of the radar.

The RCS application is primarily found in military style effect technology. It is because most military aircraft want to penetrate the enemy area without being detected. For example, if an aircraft gets detected then easily it will be destroyed by anti-aircraft missiles. So military technology primarily uses this Radar Cross-section. And apart from the military we also use in aviation technology. So, it is a very important field in

aerospace engineering. Basically, the definition of RCS is dependent on several factors for example if we have target located from radar at a distance of “R” then we can express the RCS of the target by using this equation. (RCS) $\sigma = 4*\pi*R^2 * (Pr/Pi)$. RCS is primarily measured in terms of squared meters or in the more conventional unit which is known as dBA squared meters. And it is basically the ratio of backscattered power density to the incident power density on the target. And backscattered power means the reflected power from the target to the radar receiving antenna. RCS primarily depends on the physical geometry and material and then the direction of the radar and then the polarization of the scattered signal and signal frequency as well. The value of RCS basically is a measure of how easily detectable an object is. So, the lower the value of RCS the better for military vehicles or anti-all missiles or aircrafts. They do not want to be get detected. And RCS has two classifications. One is Monostatic RCS where transmitter and the receiver antenna are located in the same place. And then we have got the Bi-Static RCS where we have several receiver antennas located at different positions and have also a transmitter antenna located at different positions

CHAPTER 2

FABRICATION PROCESS

2.1 Fabrication of Copper Rings

Copper rings with different dimensions are fabricated to be used as conductive layers in 3D-printed EM test specimens.

Small copper ring inner diameter = 3 mm

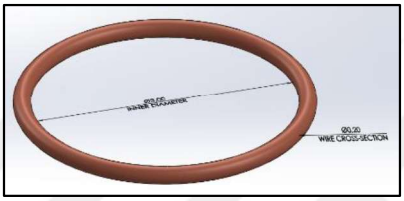

Medium copper ring inner diameter = 4.5 mm

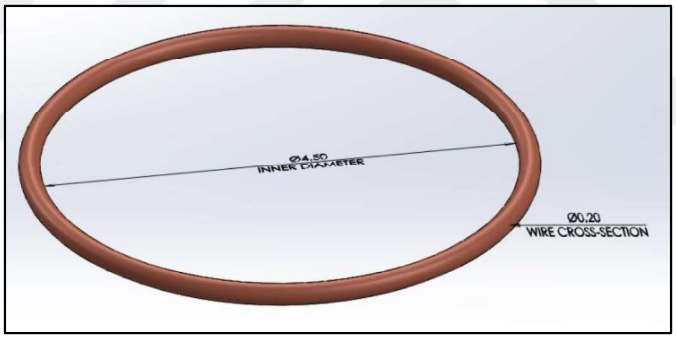

Large copper ring inner diameter = 6 mm

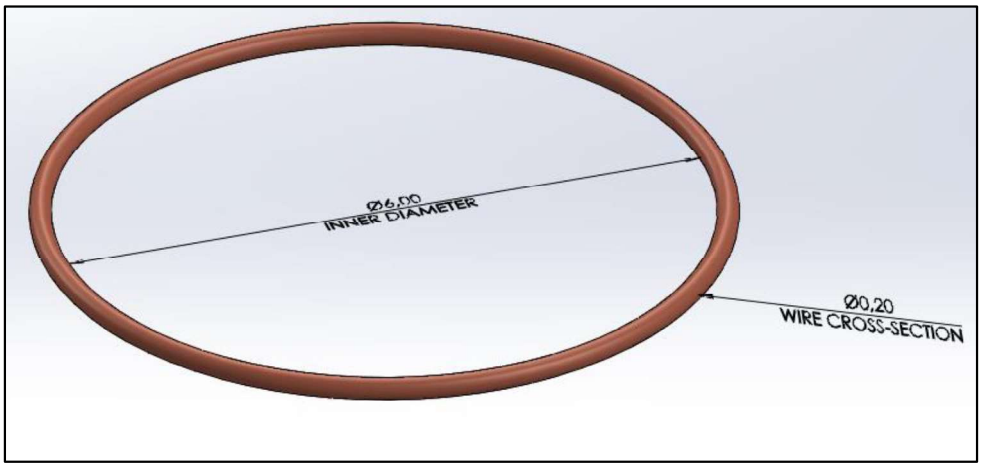

Figure 2.1 Copper rings design with the same wire cross-section and different diameters

For this purpose, copper wires with Ø 0.2 mm diameter were used. For the manufacturing process, two ends of wires were soldered together with appropriate dimensions in ring shapes as shown in the previous Figure 2.1. The resulting produced copper rings can be seen in Figure 2.2 and these rings were used as conductive parts of the designed multilayered FSS structures.

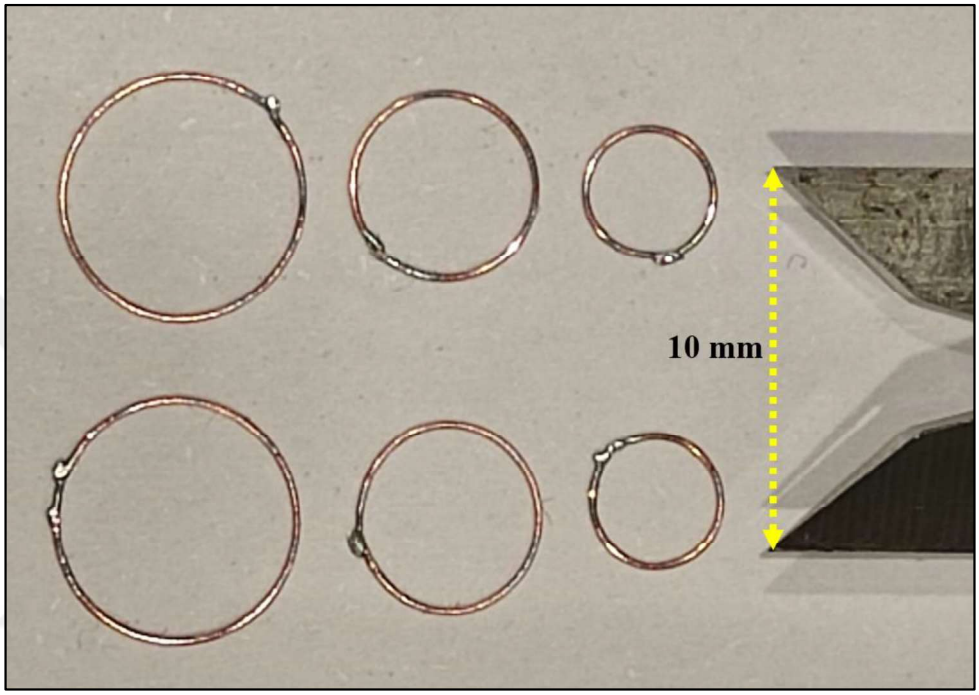

Figure 2.2 Manufactured Copper Wire Rings for Multilayer FSS Structure Tests

2.2 3D Printing Process

With the 3D Printing technology, frequency-selective surface (FSS) structures can easily be fabricated for any filtering purposes including low-pass, high-pass, and band-pass or stopband behavior with any kind of configuration. 3D-printed polymeric materials for FSS design will also have to show good mechanical behavior if the 3D-printed parts were to be used in aerospace applications as a backing of antennas and as radomes and sort. What needs to be achieved with this study is having a reduced radar cross-section through 3D-printed FSS structures with various sizes of conductive copper rings. Rings are placed on top of each layer starting from larger to a smaller diameter from bottom to top in the solid multilayered 3D fabricated test specimens shown in Figure 2.10.

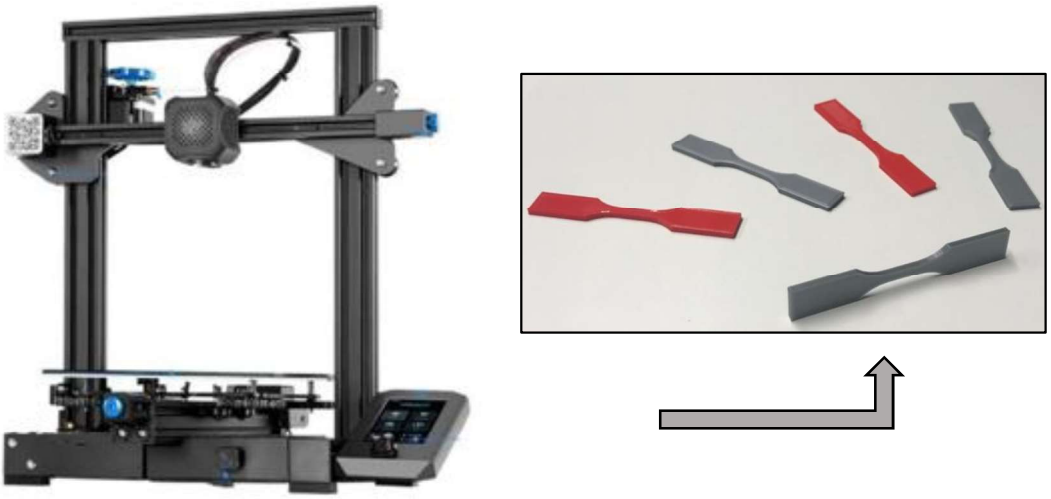

Figure 2.3 Creality3D Ender 3 v2 - for 3D printing PLA - FDM Method

In Figure 2.3, With FDM Method is used to manufacture test sample parts with PLA filament. The infill of the test specimens is built in -/+45° cross-ply orientations. It was also set to use minimum material.

Figure 2.4 Markforged-X7- for 3D printing Nylon6 FR - FDM Method

Markforged - X7 shown in Figure 2.4 is working also with FDM Method. In comparison to other 3D printers with FDM Method used in this study, Markforged-X7 had the finest nozzle tip (nozzle diameter). NYLON6-FR filament was used to build test samples. The infill orientation was not able to be selected by the user. This 3D

printer maximizes the infill with filament material. and it usually prints in -/+45º raster orientation by default.

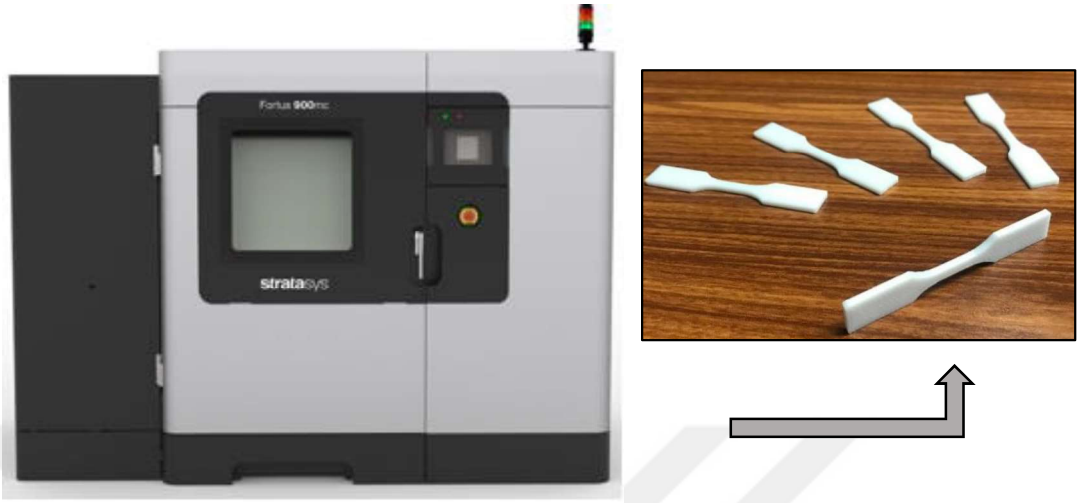

Figure 2.5 Stratasys-Fortus900mc - for 3D printing PolyCarb - FDM Method

The 3D printer in Figure 2.5 is also working with FDM Method. It is used to manufacture test samples with ULTEM 9085FR and also Poly Carbonate filaments. The infills of the test specimens are built in -/+45º cross-ply orientations as well. It was set to use minimum material.

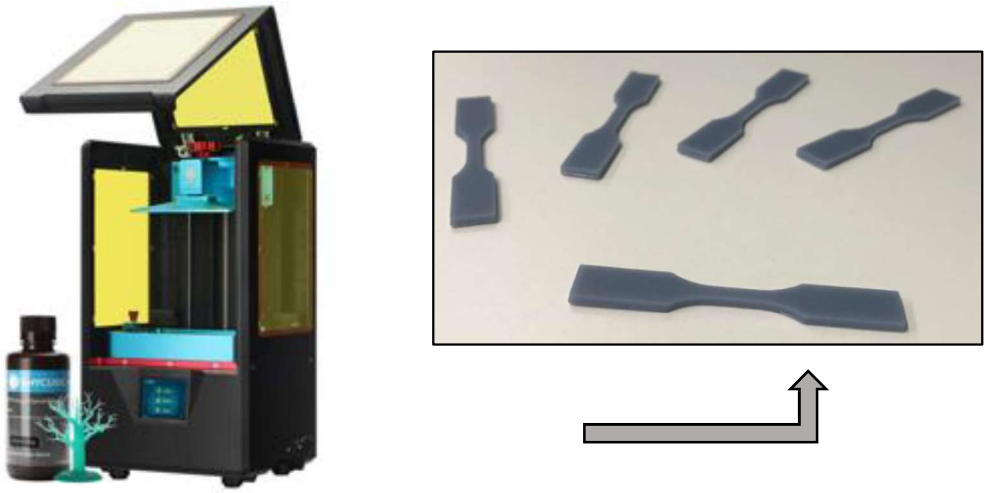

Figure 2.6 ANYCUBIC Photon S - for 3D-Printing ANYCUBIC Basic Resin - SLA Method

A liquid photo-curable basic resin is used as the base and with laser light at 405 nm wavelength, the resin solidification takes place to generate the test specimens needed for this study with the SLA Method 3D Printer illustrated in Figure 2.6.

Table 1.1 3D Printing Parameters for FDM Printers [27-29]

	3D Methods	Nozzle Temperature	Printing Bed Temperature	Layer Thicknesses	Nozzle Diameter	Filament Material
Creality3D Ender 3 v2	FDM	210 ºC	Up to 110 ºC	0.1mm - 0.4mm	0.4 mm	PLA
Markforged-X7	FDM	240 ºC	70 ºC -90 ºC	50µm - 250µm	0.4mm & 0.9mm	NYLON6-FR
Stratasys-Fortus900mc	FDM	Up to 435 ºC	Up to 235 ºC	0.254 mm	0.254 mm	PC & ULTEM9085-FR

In Table 1.1, it can be seen that the 3D printing parameters of the FDM method 3D printers. Three different FDM 3D printers are used for this study. Moreover, one SLA method 3D printer is used and its fabrication parameters are presented in Table 1.2.

Table 1.2 Printing Parameters for Stereo Lithography Apparatus [30]

	3D Method	Light Source	Rated Power	Printing Speed	Layer Resolution	Printing Material
AnyCubic Photon S	SLA	405 nm UV wavelength	50 W	20 mm/hr	25-100 nm	405 nm Basic Photo Sensitive Resin

2.2.1 3D-printed EM Test Specimens

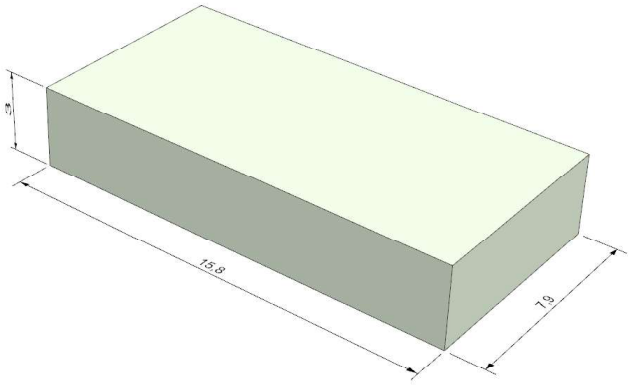

Figure 2.7 A 3D model is created with dimensions 3 mm x 7.9 mm x 15.8 mm for EM characterization test samples

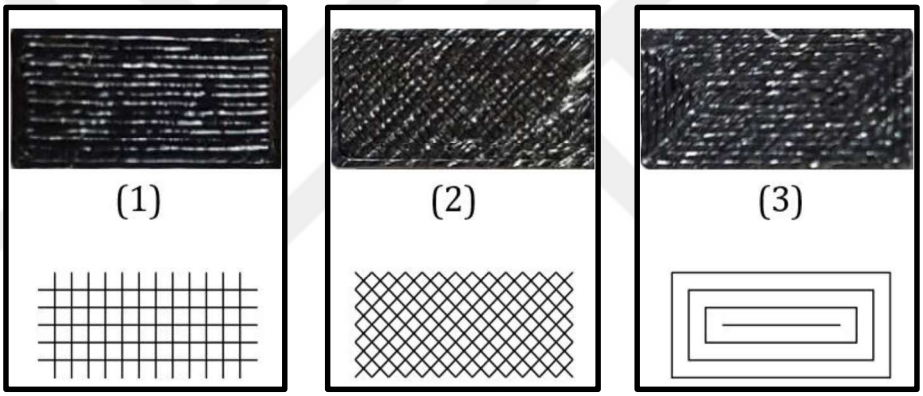

Figure 2.8 ULTEM 9085 FR (Flame Retardant) for EM Characterization (1) 0-90° cross-ply, (2) -/+45° cross-ply, (3) perimeter orientations

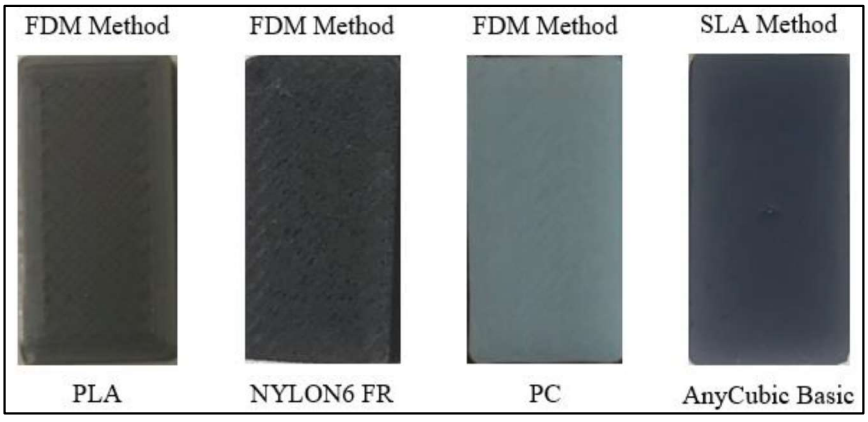

Figure 2.9 Fabricated EM Characterization Test Specimens, All FDM Methods built with -/+45° cross-ply orientation

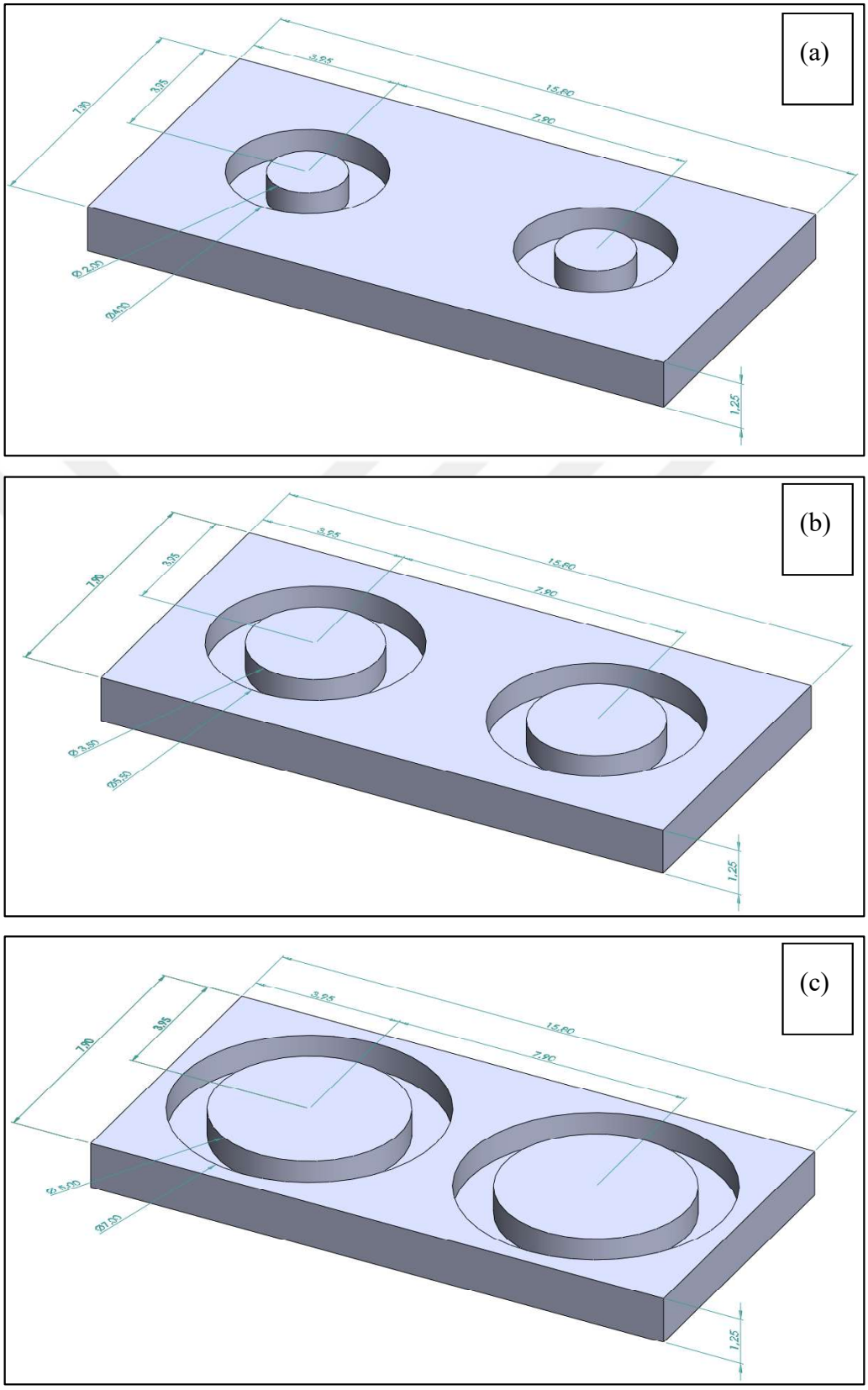

Figure 2.10 Dimensions of each 3D design model of multilayer FSS Structure with (a) Small, (b) Medium, and (c) Large size grooves respectively

The samples of ULTEM 9085 Flame Retardant and their raster orientations are illustrated in Figure 2.8 above. The rest of the EM characterization samples are fabricated in only one raster orientation shown in Figure 2.9 above. Due to insufficient materials, only small waveguide test samples of -/+45° cross-ply orientation were able to be fabricated for electromagnetic characterization tests by fused deposition modeling (FDM).

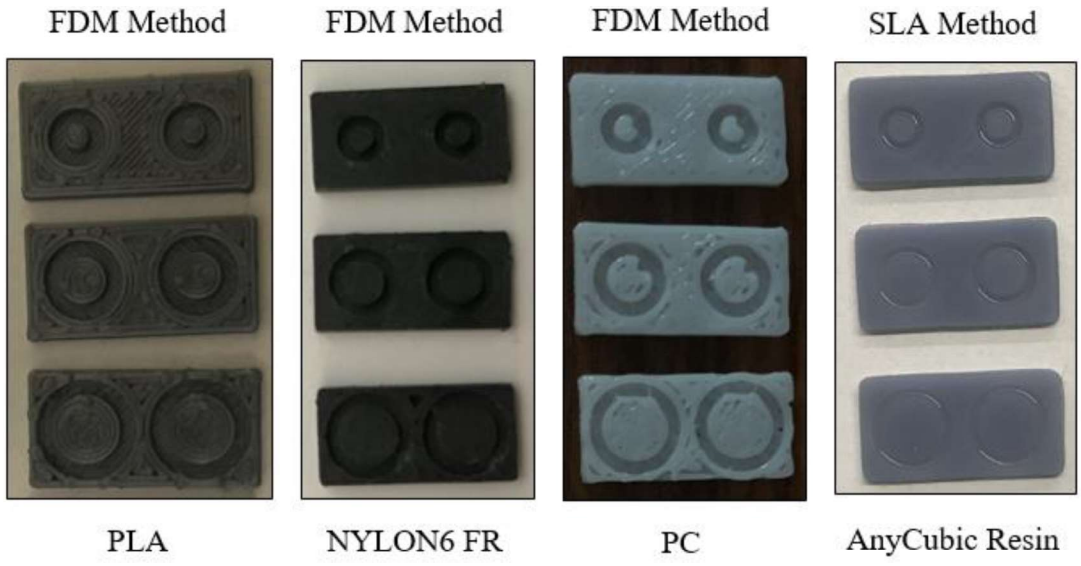

Figure 2.11 Fabricated Multilayer FSS Structure Test Specimens Empty, All FDM Method built with -/+45° cross-ply orientation, no orientation for SLA Method

The waveguide test specimens were quite small in size in order for fitting in the waveguide sample holder. It was inevitable not to have defects in the process of fabricating such small test specimens, which should stay within the boundaries of a prism of 1.25mm x 8mm x 16mm, for FDM method 3D printers (see Figure 2.10). The impurities are visible to the eye with PC and NYLON6 FR and PLA as seen in Figure 2.11 (which are built with FDM Method). Furthermore, the grooves' dimensional tolerances had to be set loose for soldered copper wire rings to fit in the 3D-printed substrates, see Figure 2.13.

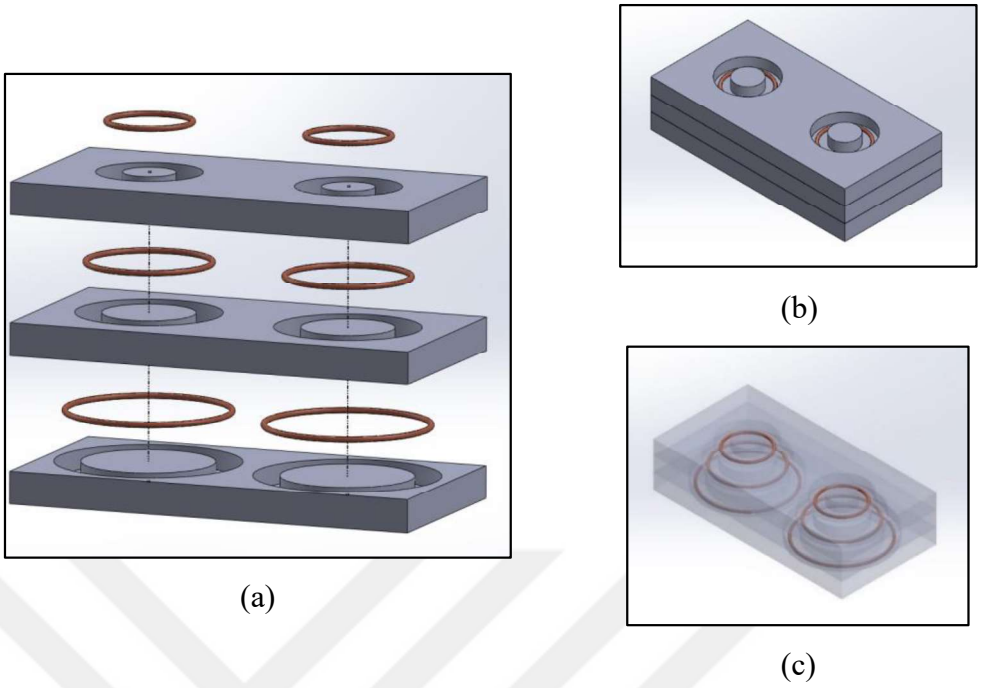

Figure 2.12 Exploded (a), Solid Assy (b), and Transparent (c) Views of Multi-layer FSS Assembly

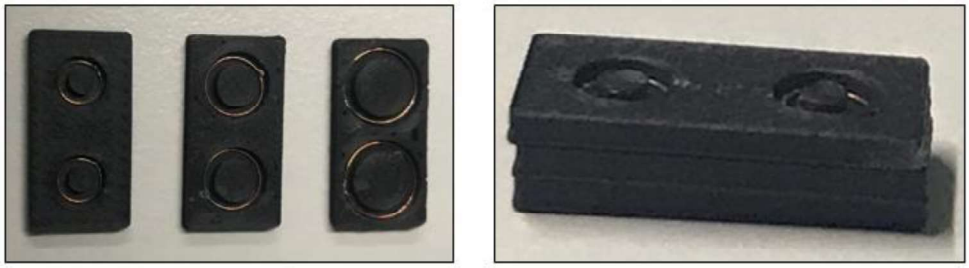

Figure 2.13 Actual Multilayered FSS Structure Assemblies for Waveguide Sample Holder

2.2.2 3D-printed Tensile Test Specimens

3D-printed test specimens are manufactured using the filaments specified in previous chapters. The sizes are determined according to ASTM D638-14 Tensile Test Standards. Due to the lack of some of the filament materials and also in order to keep the cost lowest, Type V which is the minimum size sample within this standard was chosen. Dog bone test specimens in Figure 2.15 are fabricated according to the dimensions given in Figure 2.14.

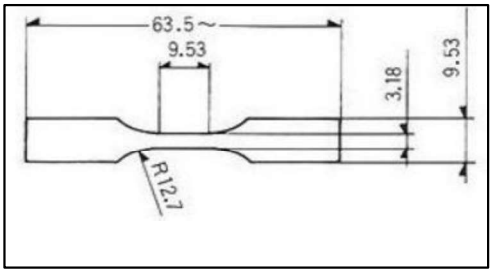

Figure 2.14 ASTM D638-14 Type V Sample Dimensions

The pictures of the manufactured samples are given in the following figures. One can see from the figures that three of the test specimens were built with the FDM method while the last one was manufactured with the SLA method in order to carry out the mechanical tensile tests to compare their mechanical strengths.

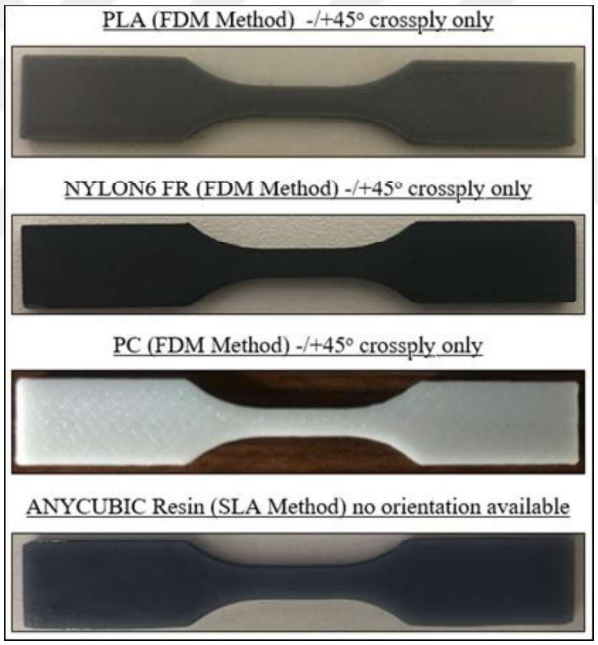

Figure 2.15 ASTM D638 - 14 Standard, Type 5 Specimens for Tensile Tests

The samples manufactured using the FDM method have -/+45° cross-ply configuration and a minimum amount of materials are used for dog bone test samples. On the other hand, there is no raster orientation applicable to manufacture ANYCUBIC (AC) Basic-Resin because the resin in the SLA method is photo-curable and is fabricated layer-by-layer by solidification with UV lights with a wavelength of 405 nm.

CHAPTER 3

MATERIALS AND METHODS

3.1 Electromagnetic Characterization of Materials

3.1.1 Scattering Parameters (S-Parameters)

Scattering parameters, shortly known as S-parameters, describe the reflected and transmitted energy between ports. For a two-port system, there are four scattering parameters as S_{11}, S_{12}, S_{21} and S_{22} as shown in the figure below.

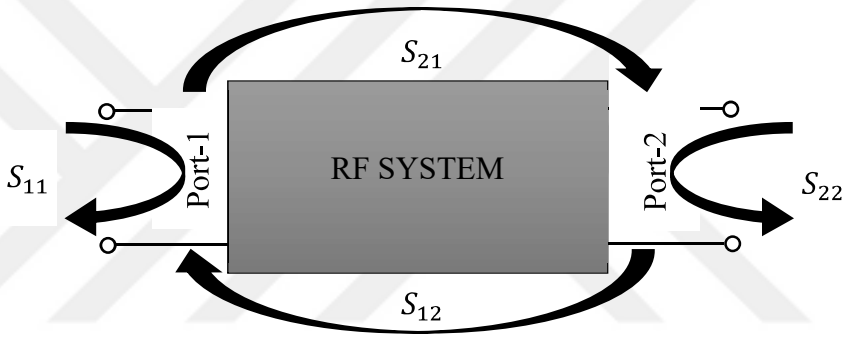

Figure 3.1 Scattering parameters for a two-port system

Here, S_{11} and S_{22} refer to the reflected signal from the port-1 and port-2, respectively. On the other hand, S_{12} and S_{21} represent the transmitted signals between the port-1 and port-2.

3.1.2 Determining complex (ε) and (μ) through S-parameters

Scattering parameters needed to be collected to calculate relative permittivity and relative permeability were measured by using a Vector Network Analyzer. The device must be calibrated at the beginning of the measurement by using metallic reference plate and air for full reflection and full transmission. There are several methods to measure scattering parameters in order to conduct electromagnetic characterization of

materials. Free-Space, Waveguide, Di-electric probe and Co-axial tube methods can be listed as the most common ones. All methods require the use of a Network Analyzer.

In Free-Space measurement method, there are two antennas faced to each other and the material to be tested is placed at the mid-point between the antennas as shown in the following figure. In this method, the calibration is also conducted using a metal plate with known thickness and air for full transmission.

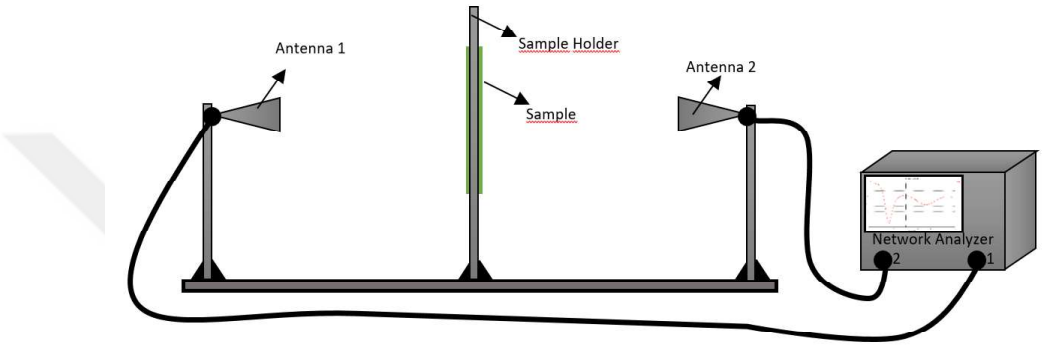

Figure 3.2 Free-Space Measurement setup for electromagnetic characterization of materials

In waveguide measurement method, the material to be tested is placed in a sample holder which is between two waveguides connected to a network analyzer as shown in the following figure.

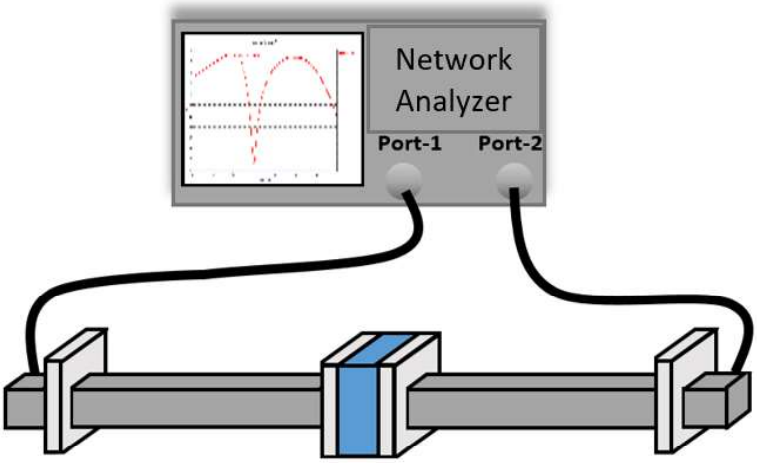

Figure 3.3 Waveguide measurement setup for electromagnetic characterization of materials

In a dielectric probe method, there is a dielectric probe connected to one port of a network analyzer. Unlike the other methods, this method is used to measure S_{11} only for liquid and semi-liquid materials. For this setup, calibration is made by using distilled water with $\varepsilon_r \approx 80$ and air with $\varepsilon_r \approx 1$. The setup is shown in the following figure.

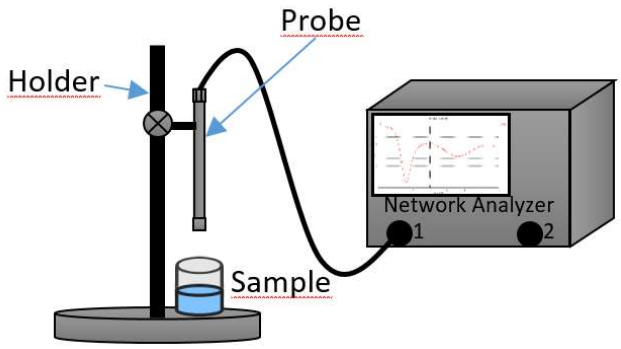

Figure 3.4 Dielectric probe measurement setup for electromagnetic characterization of materials

Coaxial tube electromagnetic measurement setup is very similar to the waveguide setup. Instead of waveguides, coaxial cables and associated sample holders are used. Ring shape samples can be tested in this setup, it is therefore easer to measure elastic materials.

In this study, waveguide setup was used and the 3D samples were prepared accordingly. The sample sizes were selected to fit a waveguide operating at Ku band which is 7.9 x 15.8 mm.

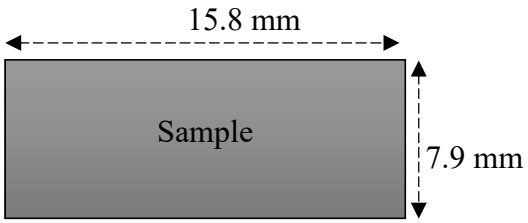

Figure 3.5 Sample sizes for waveguide setup operating at Ku band

3.1.3 Electrical permittivity (ε) and magnetic permeability (μ)

After obtaining the scattering parameters, relative electrical permittivity and magnetic permeability of materials can be written as [23];

$$\varepsilon_r = \varepsilon_r' - j\varepsilon_r'' \quad \text{and} \quad \mu_r = \mu_r' - j\mu_r'' \tag{3.1 \& 3.2}$$

Here, ε_r'' refers to the dielectric loss and μ_r'' represents the magnetic loss. At this point, it will be beneficial to mention about the relative permittivity of some materials.

Table 3.1 Relative permittivities (ε_r) of some materials

Material	ε_r	Material	ε_r	Material	ε_r
Air	1.0006	Silica	3.8	Rubber	3.0
Paper	3.0	Silicon	11.8	Ethyl Alcohol	25
Water (Distilled)	81	Nylon	3.5	Glass	6.0

It should be noted that the thickness of the reference plate (t_m) and measured specimen (t_s) were taken into consideration during the calculation procedure as given the equations below.

$$S_{11}^{cal} S_{22}^{cal} e^{-2\gamma_0(t_s - t_m)} - S_{11}^{cal} S_{22}^{cal} e^{-2\gamma_0 t_s} = \frac{\Gamma^2 - \mathrm{T}^2}{1 - \Gamma^2 \mathrm{T}^2} \tag{3.3}$$

$$e^{-\gamma_0 t_s} \frac{S_{21}^{cal} + S_{12}^{cal}}{2} = \frac{T(1-\Gamma^2)}{1-\Gamma^2 \mathrm{T}^2} \tag{3.4}$$

$$\Gamma = \frac{\mu_r^* - \sqrt{\mu_r^* \varepsilon_r^*}}{\mu_r^* + \sqrt{\mu_r^* \varepsilon_r^*}} \tag{3.5}$$

$$T = e^{-\gamma t_s} \tag{3.6}$$

$$\gamma_0 = \sqrt{-k_0^2} \tag{3.7}$$

$$\gamma = \sqrt{-\mu_r^* \varepsilon_r^* k_0^2} \tag{3.8}$$

$$k_0 = \frac{2\pi}{\lambda_0} \tag{3.9}$$

To solve the equations that are sequenced above, Newton's iteration algorithm is applied to calculation procedure. Then, imaginary parts of permittivity and permeability are also computed with respect to initial estimation of ε_r^* and μ_r^*. Overall equation can be represented as a Jacobian matrix form in following equations [23].

$$\begin{bmatrix} \frac{\partial F}{\partial \varepsilon_r^*} & \frac{\partial F}{\partial \mu_r^*} \\ \frac{\partial G}{\partial \varepsilon_r^*} & \frac{\partial F}{\partial \mu_r^*} \end{bmatrix} \cdot \begin{bmatrix} \Delta\varepsilon_r^* \\ \Delta\mu_r^* \end{bmatrix} = \begin{bmatrix} F \\ G \end{bmatrix} \tag{3.10}$$

$$F = (1 - \Gamma^2 \mathrm{T}^2)\left(S_{11}^{cal} S_{22}^{cal} e^{-2\gamma_0(t_s - t_m)} - S_{11}^{cal} S_{22}^{cal} e^{-2\gamma_0(t_s)}\right) - (\Gamma^2 - \mathrm{T}^2) \tag{3.11}$$

$$G = (1 - \Gamma^2 \mathrm{T}^2)\left(e^{-\gamma_0 t_s} \frac{S_{21}^{cal} + S_{12}^{cal}}{2}\right) - \mathrm{T}(1 - \Gamma^2) \tag{3.12}$$

$$J\Delta X = Y \tag{3.13}$$

$$\Delta X = J^{-1} Y \tag{3.14}$$

$$X^{new} = X^{old} - J^{-1} Y \tag{3.15}$$

Initial estimation of ε_r^* and μ_r^* are iterated up to a point at which $X^{new} \approx X^{old}$ is equally obtained. At the end of this iteration, calculated values are found as relative permittivity and relative permeability. Flowchart of computation method is also illustrated in Figure 3.

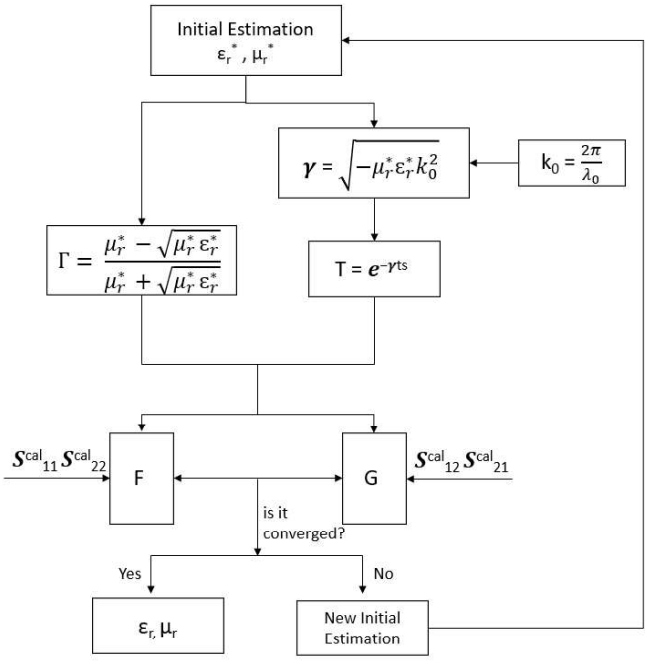

Figure 3.6 Computation Flowchart

In this flow chart ε_r is relative permittivity, μ_r is relative permeability, k_0 is wavenumber in air, γ_0 is propagation constant in free space, γ is propagation constant in specimen, Γ is reflection coefficient at air/specimen interface and T corresponds to transmission coefficient.

3.2 Design and Analysis of FSS

Once the electrical permittivity and magnetic permeability values are calculated, the corresponding EM material properties can be transferred into the computer environment. The next step is the design of the frequency-selective surface (FSS) and the metamaterial structure. In this study, we have designed a circular FSS providing a band-pass filtering property. The shape and dimensions of this structure can be seen in the following figure (Figure 3). The dimensions of the structure were chosen so that the filtering behavior occurs at around f=12 GHz. For the metamaterial part, we have used circular split ring resonators (CSRR) with the dimensions providing absorption behavior in the range of f=15-20 GHz. The detailed dimensions of the CSRR FSS can also be seen in the following figure (Figure 3).

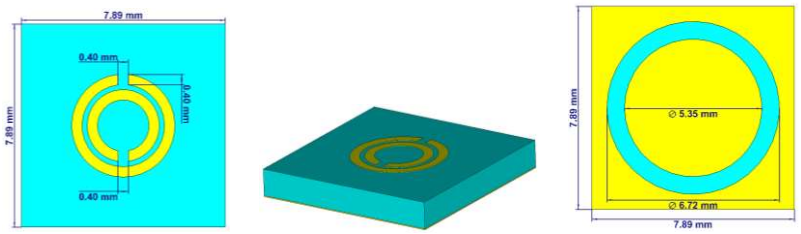

(a) (b) (c)

Figure 3.7 Copper CSRR (a) as the top layer, perspective of the structure (b), and copper circular FSS (c) at the bottom layer.

The structure is composed of three layers including the FSS layer at the bottom, a dielectric layer in the middle section, and the MTM layer at the top layer of the structure. FSS cell is simply a ring removed from a copper ground with the dimensions of R1=6.72 mm and R2=5.35 mm where R1 refers to the outer diameter while R2 is the inner diameter. This is designed so that it reflects all the signals but signals having frequencies at about 12 GHz will only pass through. FSS structure acts as a band-pass filter operating at that certain frequency point. On the other hand, the MTM structure integrated on top of the structure is composed of a split ring resonator as seen in the figure above (Figure 3.7). The thickness of the substrate was chosen as 1.6 mm while the copper thickness is 0.035 mm.

In terms of the absorption perspective, we should note that absorption is directly related to transmission and reflection. The following equation summarizes these relations between them.

$$A(w) = 1 - R(w) - T(w) \tag{3.16}$$

Here, $A(w)$ is the frequency-related absorption, $R(w)$ and $T(w)$ are the frequency-dependent reflection and transmission behaviors, respectively. In addition, reflection and transmission behavior can be written as $R(w) = |S_{11}|^2$ and $T(w) = |S_{21}|^2$ respectively using scattering parameters. In order to have high absorption, reflection and transmission must be minimized. In most absorber studies, transmission response is minimized and even eliminated by placing a metal ground plane at the back of the

structures. In our case, this task is performed by the copper sections of the FSS part placed at the bottom layer of the structure.

In the second approach, the ground plane of the antenna is changed by a multilayer frequency-selective surface with circular ring resonators as shown in Figure 3.8 below.

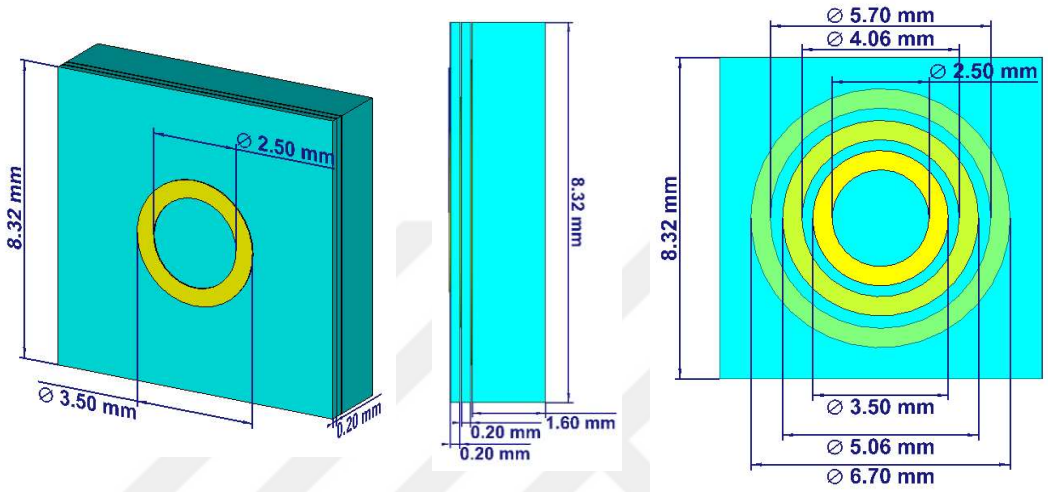

Figure 3.8 Dimensions and different views of multilayered FSS structure

The Frequency-selective Surface (FSS), which is the main focus in this thesis, is composed of three separate rings with three different dimensions. As the interlayer (substrate), 3D-printed materials were preferred instead of FR-4 dielectric material, which is a commonly used substrate for such structures. The thickness of the substrate is 1.6 mm and the material thickness between different layers was selected as 0.20 mm with the use of the 3D-printed substrates. Because of the polarization independency and better performance behaviors, the ring type of structure was preferred.

3.3 Mechanical Test Methods

All manufactured plastics/polymers are subjected to mechanical loads during the course of their operational lifetime. Concerning avoiding mechanical failure, it is crucial to evaluate the quality of the mechanical properties and regularly check them to make sure the material is fit for the intended use. In this case, one of the most

common mechanical testing methods is tensile testing in order to characterize the mechanical properties and allowables of the selected plastic materials.

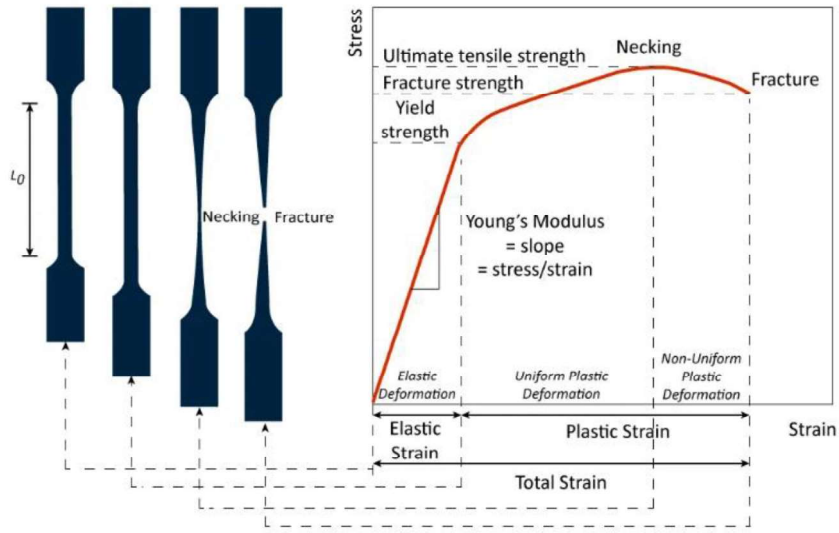

Figure 3.9 Stress-Strain plot and Necking phenomena in tensile testing [25].

$$E = \frac{\Delta\sigma_{axial}}{\Delta\varepsilon_{axial}} \tag{3.17}$$

Where E refers to Young's Modulus. In the stress-strain curve, the linear section of the graph is used to obtain axial stress and strain values. The slope of the linear curve gives us Young's Modulus which is the proportion of $\Delta\sigma_{axial}$ (Stress) and $\Delta\varepsilon_{axial}$ (Strain).

$$\sigma_{axial} = \frac{F}{A_0} \tag{3.18}$$

Where F is the force applied on the specimen and A_0 is the initial cross-sectional area.

$$\varepsilon_{axial} = \frac{\Delta L}{L_0} = \frac{L_f - L_0}{L_0} \tag{3.19}$$

Where L_f refers to the final length while L_0 is the initial length of the test specimen.

$$\sigma_{ultimate} = \frac{P_{max}}{A_0} \tag{3.20}$$

Where P_{max} is the maximum load that the specimen can withstand, A_0 is the initial cross-sectional area of the tensile specimen with these values we can calculate ultimate tensile strength ($\sigma_{ultimate}$) as shown in the equation above.

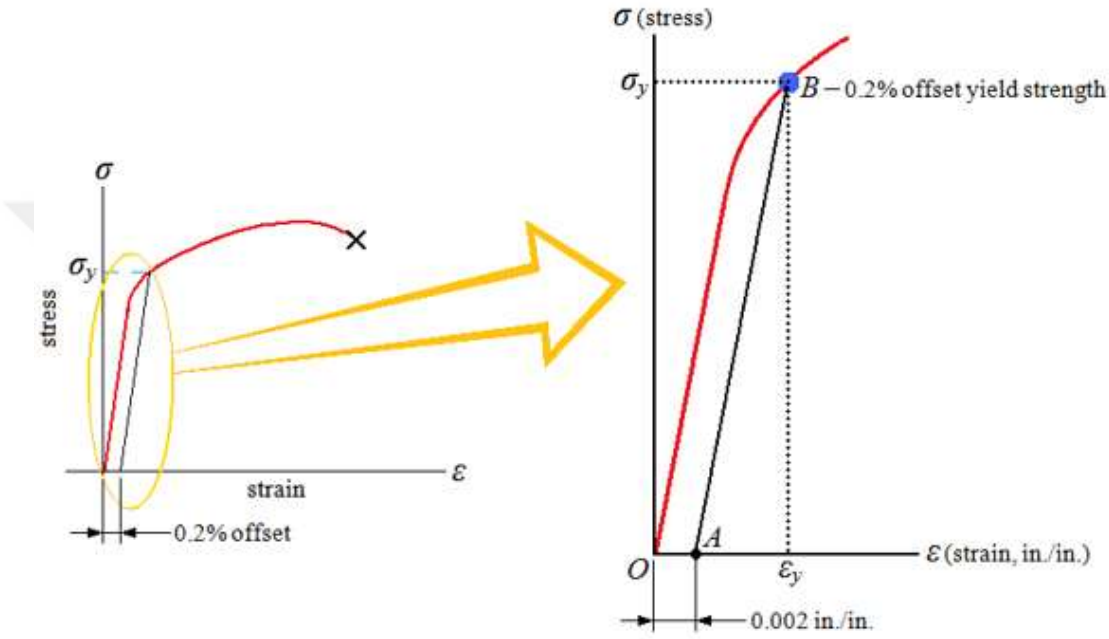

Figure 3.10 Stress-Strain Curve with 0.2% Offset [26].

A conventional method of materials test is known as tensile testing. It involves applying a controlled tension force to the test specimen until it snaps. Tensile testing of plastics is an action of stretching a plastic dog-bone specimen apart with a continuously increasing force. As the force goes up the stress on the specimen linearly increases. The slope of the linear line in the stress-strain curve gives the elastic modulus of the material. So, the stress-strain ratio is a constant in this area which satisfies Hooke's Law.

After reaching a certain point in the stress-strain curve the specimen starts plastically deformed. The initiation of this deformation is called yielding. By using the 0.2% offset methodology, yield strength on the curve can be determined. A line parallel to

the elastic linear curve can be drawn next to the elastic region. The point where the line intersects with the stress-strain curve is accepted as the yield point. Then the yield strength of the material can be obtained by that yield point on the stress-strain curve. As the load is continuously applied pulls the specimen apart, the specimen elongates until it breaks. It is when tensile testing stops at the moment of the breaking of the specimen at the maximum force. Ultimate tensile stress values can be calculated using the ratio of maximum force and initial cross-sectional area of the narrow section/gage section of the dog bones. Ultimate tensile stress can also be obtained from the stress-strain curve. The highest stress point on the curve gives the ultimate stress value.

3.3.1 Tensile Test Specimens

Test Specimens are designed and manufactured according to ASTM D638-14 standards for tensile testing of plastics. Type V dog bone tensile test specimen is selected due to its smaller size and a high number of specimens needed (5 pieces dog bone) for each different 3D-printed material. The dimensions of the type V tensile test specimens are given in the figures and tables below in millimeters.

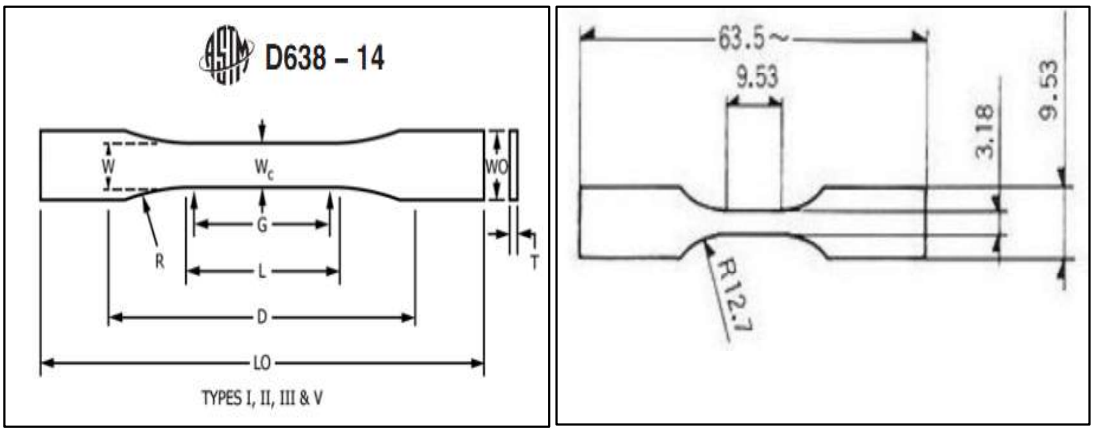

Figure 3.11 ASTM D638 Type V (with an average thickness of 3 mm)

Table 3.2 ASTM D638-14 Type V for Test Specimen Dimensions

Dimensions (see drawings)	Specimen Dimensions for Thickness, *T*, mm (in.)[A]	
	4 (0.16) or under	
	Type V[C,D]	Tolerances
W—Width of narrow section[E,F]	3.18 (0.125)	±0.5 (±0.02)[B,C]
L—Length of narrow section	9.53 (0.375)	±0.5 (±0.02)[C]
WO—Width overall, min[G]	...	+ 6.4 (+ 0.25)
WO—Width overall, min[G]	9.53 (0.375)	+ 3.18 (+ 0.125)
LO—Length overall, min[H]	63.5 (2.5)	no max (no max)
G—Gage length[I]	7.62 (0.300)	±0.25 (±0.010)[C]
G—Gage length[I]	...	±0.13 (±0.005)
D—Distance between grips	25.4 (1.0)	±5 (±0.2)
R—Radius of fillet	12.7 (0.5)	±1 (±0.04)[C]
RO—Outer radius (Type IV)	...	±1 (±0.04)

Five samples of each 3D-printed material were manufactured. Each sample's dimensions were measured and average dimensions were calculated and tabulated in the table below. The table includes the thickness of the samples, width, and length of the gage section of the dog bone Type V specimens and the cross-sectional area.

Table 3.3 Tabulated data of measured dimensions Type V ASTM D638-14

	Average Measured Dimensions of Gage Area			
Samples	T-thickness of the specimen (mm)	W-width of gage section (mm)	L-length of gage section (mm)	A_0-Cross-sectional area (mm^2)
PLA	1,926	3,324	9,582	6,402
NYLON 6 FR	2,012	3,292	9,546	6,624
Poly Carbonate	2,162	3,180	9,522	6,875
ANYCUBIC Basic	2,148	3,333	9,570	7,157

For a better understanding, the common stress-strain curve for the tensile test is given in Figure 3.12. When the tensile load is applied on a test specimen, a linear line is obtained in the stress-strain curve which shows the elastic region. In addition, the slope of the linear curve in an elastic region which is $\frac{\Delta\sigma}{\Delta\varepsilon}$ that gives the elastic modulus (Young's Modulus) of the test specimen material. The maximum stress on this linear

curve is called yield stress. After the yield stress point, the test specimen starts deforming permanently. The region with deformation is called the plastic region until the point of the breakage of the test specimen. The maximum stress point on the plastic region indicates the ultimate strength of the specimen. The deformation that occurs after ultimate tensile stress causes necking to the test specimen until fracture.

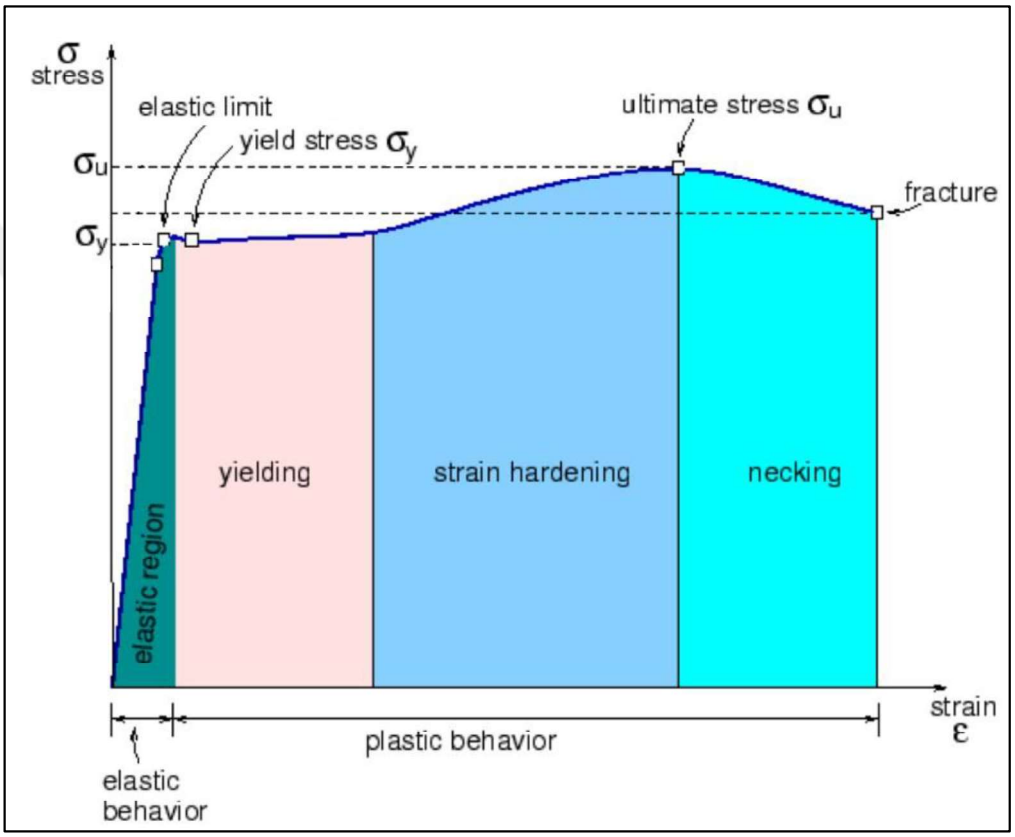

Figure 3.12 Stress-Strain Curve [24]

3.3.2 Tensile Test Setup

Instron Servohydraulic 8802 will be used as a universal testing system to perform the tensile tests. Used for dynamic, fatigue, and static testing on a wide range of materials and components. As mentioned above the specimens' form and sizes are given according to ASTM D638 Standards. Each 3D-printed specimen will be tested individually with this testing setup. The test specimen is loaded with an axial force stretching it apart. This tensile test is a destructive method so that the specimens will be broken at the end of the test.

Throughout a standard tensile test, a specimen in the shape of a dumbbell or dog bone is gripped at both ends and pulled apart to elongate until it reaches its breakpoint. It features a variable pulling rate and a maximum dynamic load of 250 kN. According to the ASTM standard, the experiment's configuration might be altered to meet various types of mechanical testing such as compression test fatigue test, dynamic test, etc.

Figure 3.13 Tensile Test Setup Instron Servohydraulic 8802

Five dog bone samples of each 3D-printed material were mechanically tested with a speed rate of 1 mm per minute. The results will be mentioned in the results and discussion section. It can be seen how a Type V tensile test specimen is installed on a universal testing system.

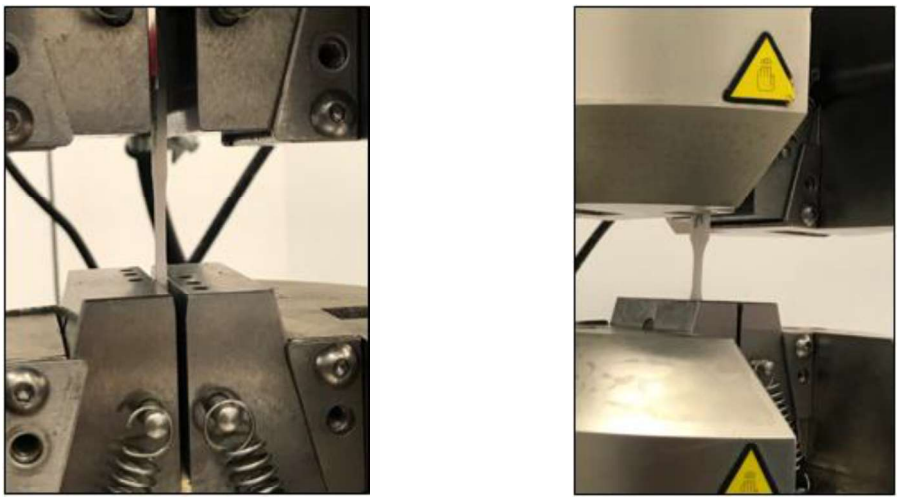

Figure 3.14 Tensile Test Specimen Installation

CHAPTER 4

RESULTS AND DISCUSSIONS

4.1 Electromagnetic Test and Simulation Results

4.1.1 FSS+MTM Analysis

The manufactured 3D samples were measured in the waveguide system and the obtained results for their electromagnetic characterization are given in the following figures. In Figure 4.1, the real parts of the electrical permittivity values are given for all specimens. Other than NYLON6FR, the rest of the specimens have almost constant values over the entire frequency band (12-18 GHz).

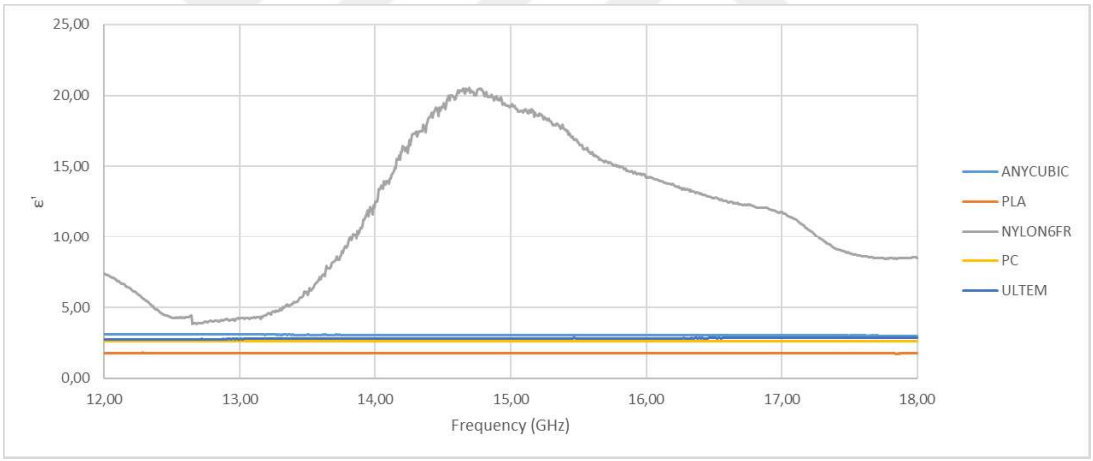

Figure 4.1 Electrical Permittivity values of the 3D-printed samples

In order to show the magnetic properties of the specimens, real parts of the complex magnetic permeability values were also determined in the same test setup and shown in Figure 4.2. Similarly, all samples have approximately constant values except for the NYLON6FR material. This type of behavior indicates that the electrical and magnetic responses are strongly related to the operating frequency of the system.

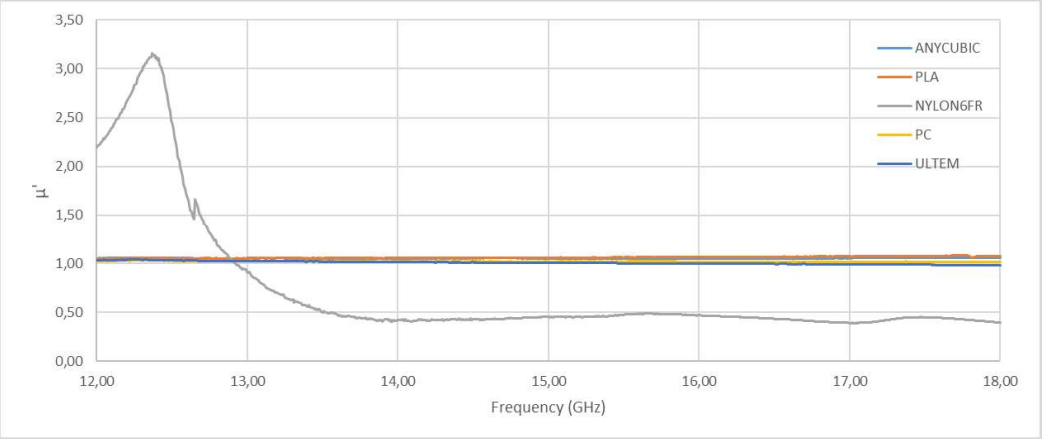

Figure 4.2 Magnetic Permeability values of the 3D-printed samples

For the first case for reducing RCS caused by antennas, the combinations of FSS and MTM structure using three different 3D-printed substrates are tested and the resulting reflection, transmission, and absorption graphs are drawn in this section. In this part, three different raster orientations using ULTEM 9085 FR (Flame Retardant) as shown in Figure 2.8 (from section 2.2.1). In this case, Sample-1 refers to 0-90° cross-ply orientation, Sample-2 refers to -/+45° cross-ply orientation, and Sample-3 refers to the perimeter orientation.

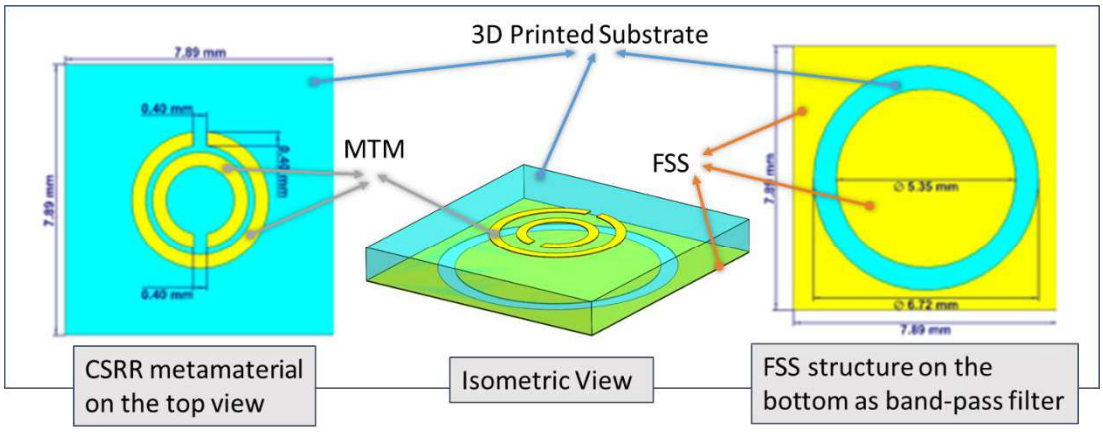

Figure 4.3 Structural Design of MTM+FSS as antenna backplate

In the first case, Sample-1 was used as the substrate and the obtained graphs are shown below in Figure 4.4. As seen in the figure, band-pass behavior is present at around

f=12 GHz while the reflection and transmission stay low after f=15 GHz resulting in a good absorption behavior (Figure 4.7).

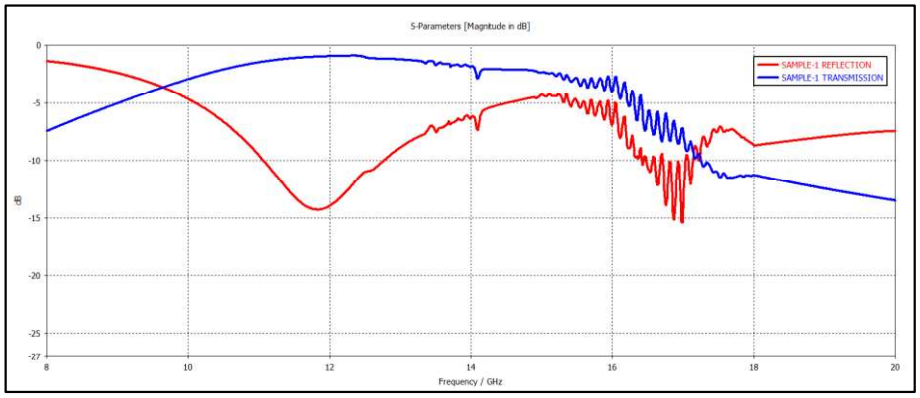

Figure 4.4 Reflection and transmission of the structure for ULTEM 9085FR Sample-1 (Amplitude in dB vs Frequency in GHz)

The same approach was applied to all three samples and the reflection along with transmission behaviors are given in Figure 4.5 and Figure 4.6 for the second and third samples, respectively. One can see from the figures that the filtering operation works well at f=12 GHz with reflection magnitudes of approximately -12.5 dB for both cases. In addition, the transmission values are very close to 0 dB at f= 12 GHz, meaning that there is no electromagnetic wave transmission between two ports at these frequency points. Besides, the absorption behavior can also be seen at higher frequencies, similar to Sample-1.

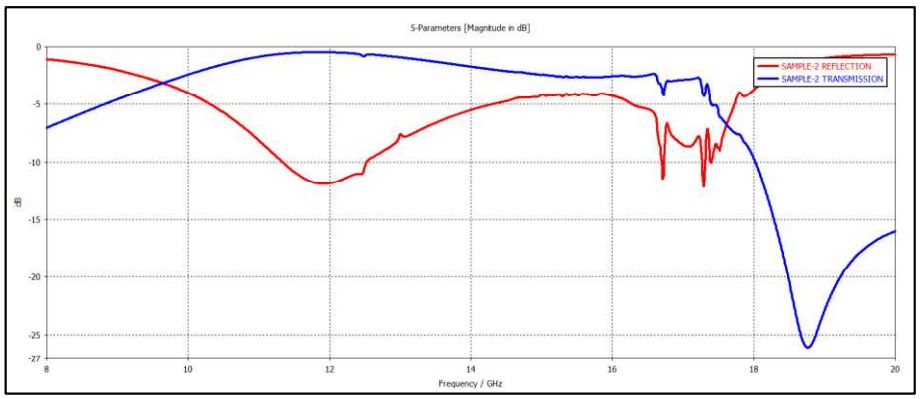

Figure 4.5 Reflection and Transmission of the structure for ULTEM 9085FR Sample-2

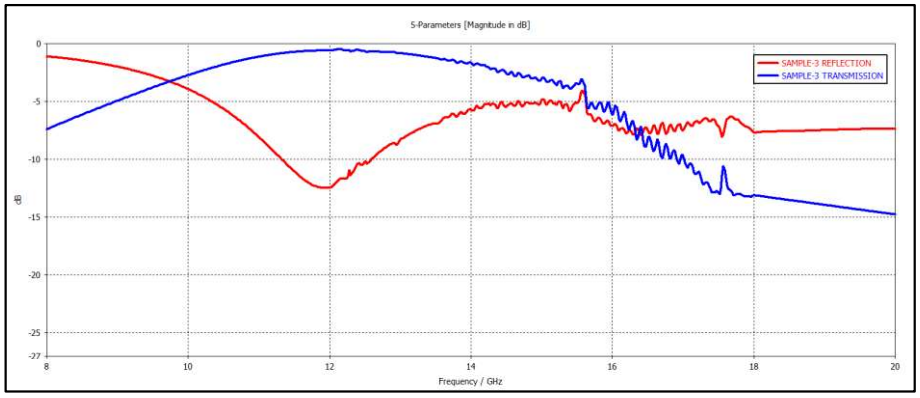

Figure 4.6 Reflection and Transmission of the structure for ULTEM 9085FR Sample-3

For a better understanding, the absorption graphs have been drawn for all three cases in terms of frequency bands (Figure 4.4-4.6). In the figures below, the x-axis refers the frequency in GHz while the y-axis represents the absorption level (where 1 stands for 100% absorption). In Figure 4.7 and Figure 4.9, the absorption values are very close to 80%, whereas in Figure 4.8, the absorption value is almost 70% top as expected from the reflection and transmission graphics for all three samples. As a result, samples with 0° / 90° cross-ply and perimetric orientation provided higher absorption values for higher frequencies (smaller wavelength). However, the sample with -45°/+45° cross-ply orientation shows slightly less absorption behavior compared to the other samples.

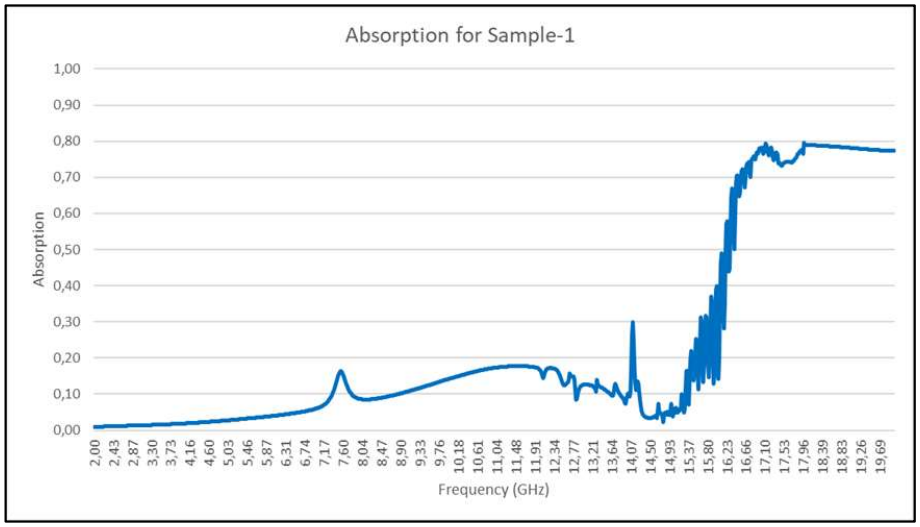

Figure 4.7 Absorption of MTM+FSS structure for ULTEM 9085FR Sample-1 with respect to wavelength

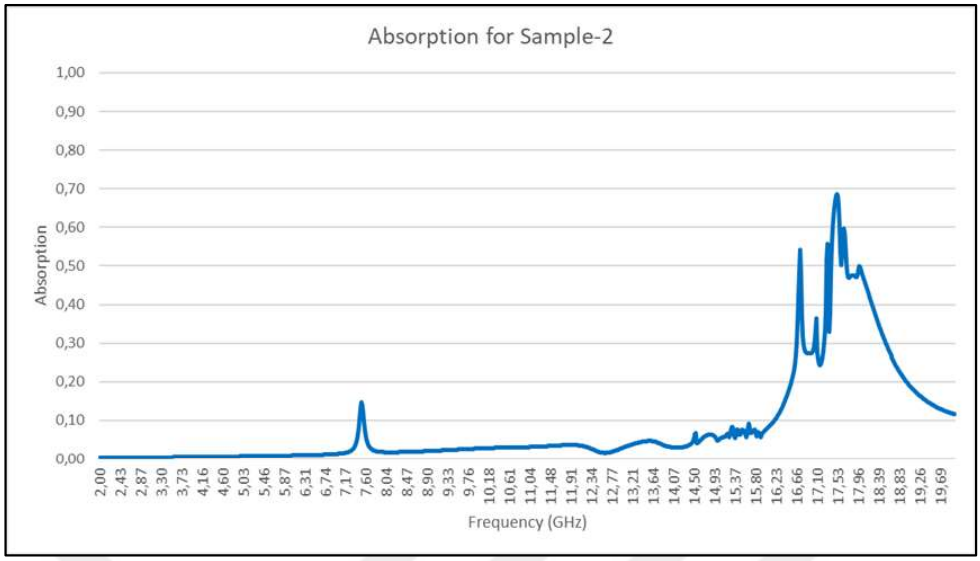

Figure 4.8 Absorption of MTM+FSS structure for ULTEM 9085FR Sample-2 with respect to wavelength

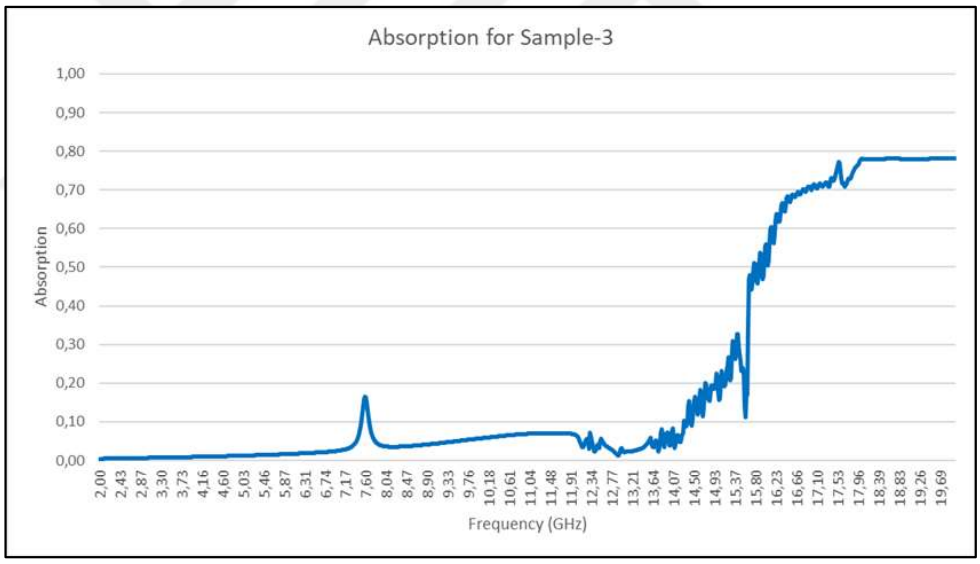

Figure 4.9 Absorption of MTM+FSS structure for ULTEM 9085FR Sample-3 with respect to wavelength

Electromagnetic characterization tests are conducted for the rest of the 3D-printed materials. Scattering parameters are obtained by waveguide test setup then electrical permittivity (ε) and magnetic permeability (μ) values are derived. With these values, the reflection and transmission curves are presented for MTM+Substrate+FSS structures in the graphs below for dielectric substrates of Polycarbonate (Figure 4.10),

PLA (Figure 4.11), and NYLON6-FR (Figure 4.12) that are all built by FDM method and only single raster angle orientation is used for fabrication which is +/- 45° angle cross-ply. ANYCUBIC substrate is fabricated by the SLA method. Basically, photo-curable liquid is solidified layer-by-layer (raster does not apply to this method). The reflection and transmission curves for ANYCUBIC are presented in Figure 4.13.

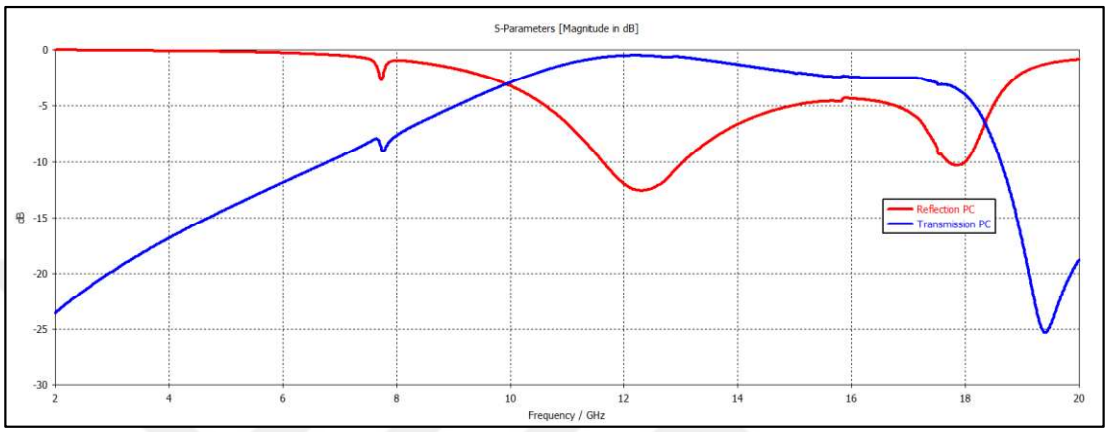

Figure 4.10 Reflection and transmission of the structure for PolyCarbonate

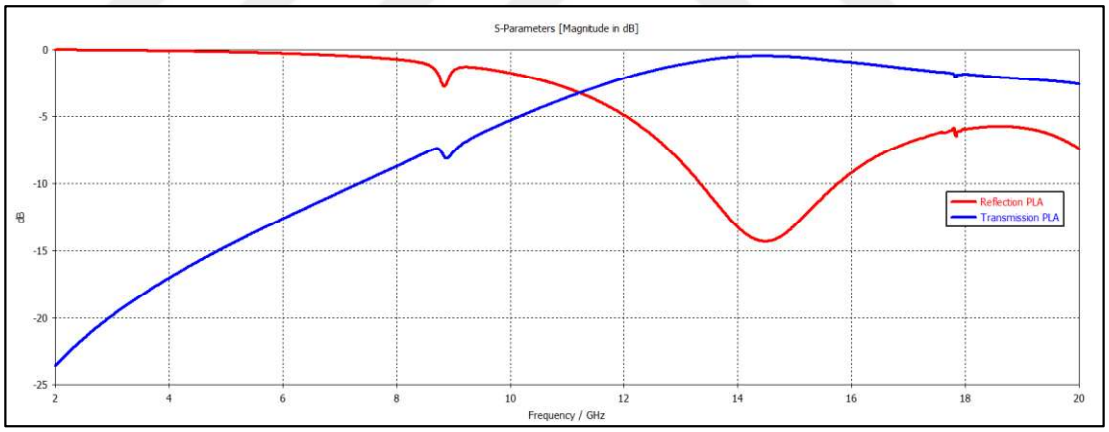

Figure 4.11 Reflection and transmission of the structure for PLA

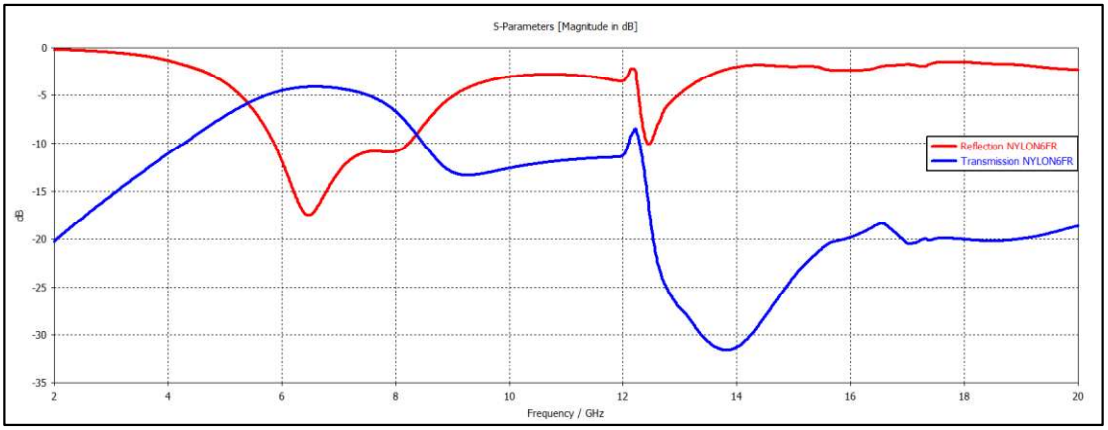

Figure 4.12 Reflection and transmission of the structure for NYLON6-FR

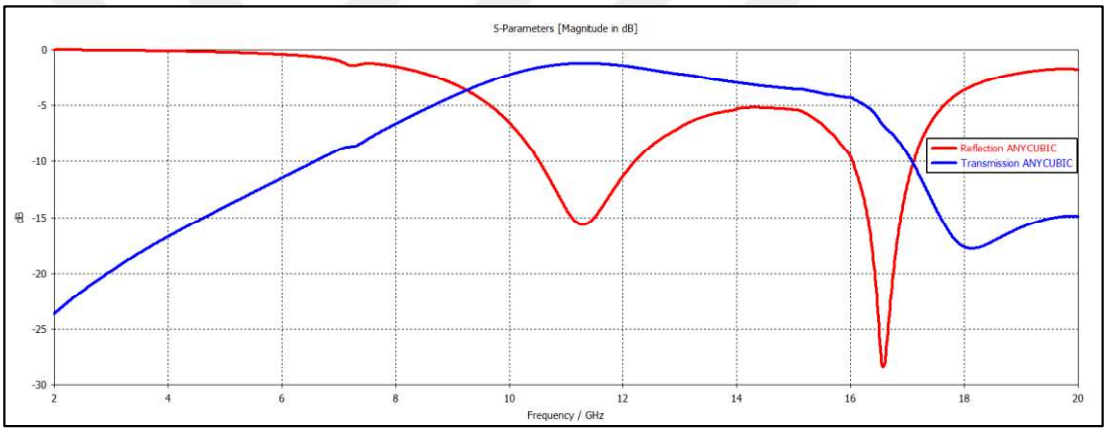

Figure 4.13 Reflection and transmission of the structure for ANYCUBIC Resin

The purpose of this study with MTM+FSS was to obtain good amount absorption values. When the magnitude of both reflection and transmission values are below zero at the same time, displayed in S- Parameter (dB) vs Frequency (GHz) graphs (in Figure 4.10-4.13). EM waves are expected to not get reflected and transmitted. Thus, this indicates that the waves are absorbed. The degrees of absorption in percentages are illustrated in the figures below in Figure 4.14-4.17.

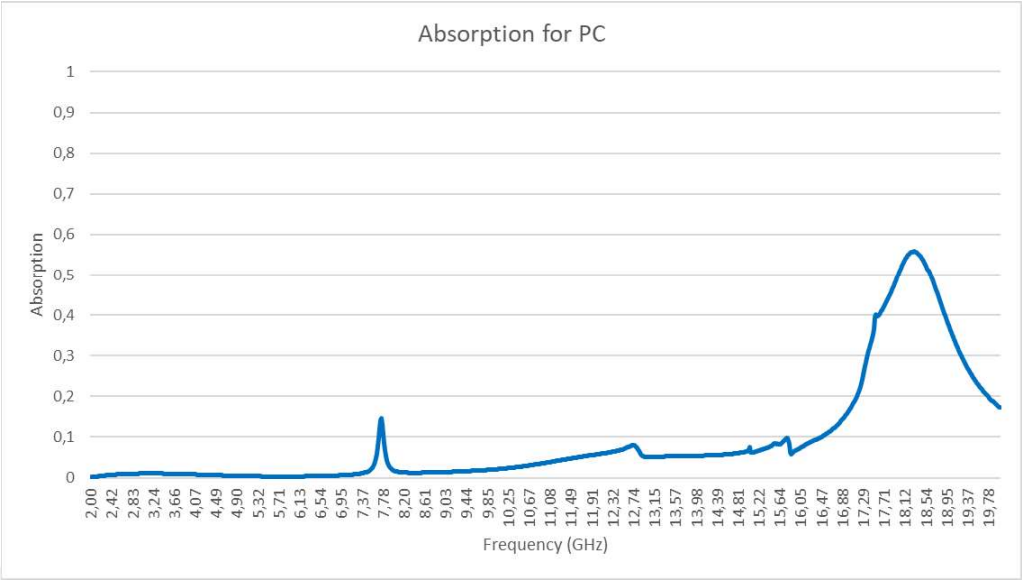

Figure 4.14 Absorption of MTM+FSS structure for PC

The dielectric properties of the PC substrate after characterizations tests was showing very good dielectric behavior. When the PC is composed of circular split ring resonator (CSRR) metamaterials (MTM) and frequency-selective surfaces (FSS) the amount of maximum absorption reaches 56% at around 18.4 GHz of frequencies.

These results are the outcomes of EM simulations.

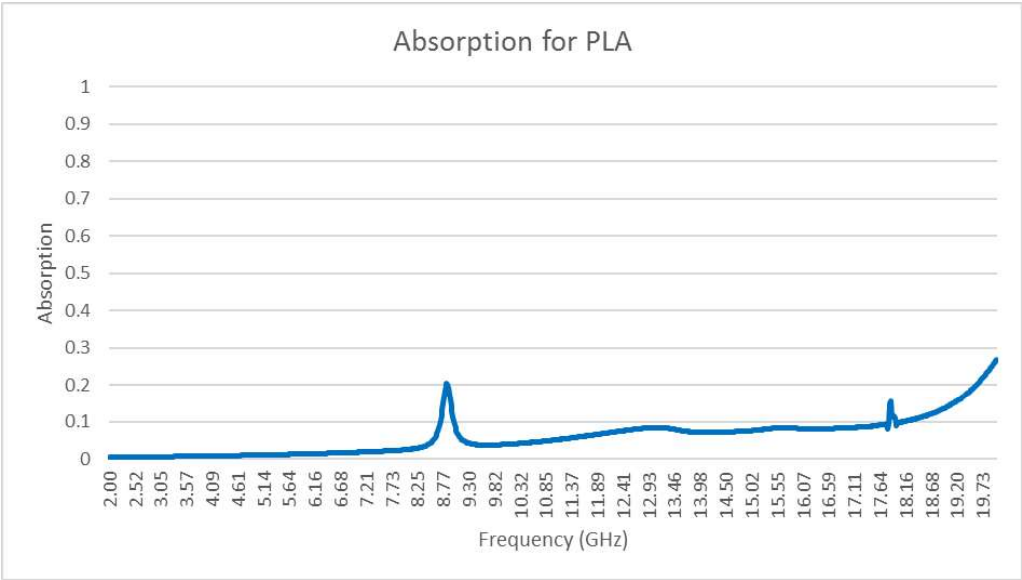

Figure 4.15 Absorption of MTM+FSS structure for PLA

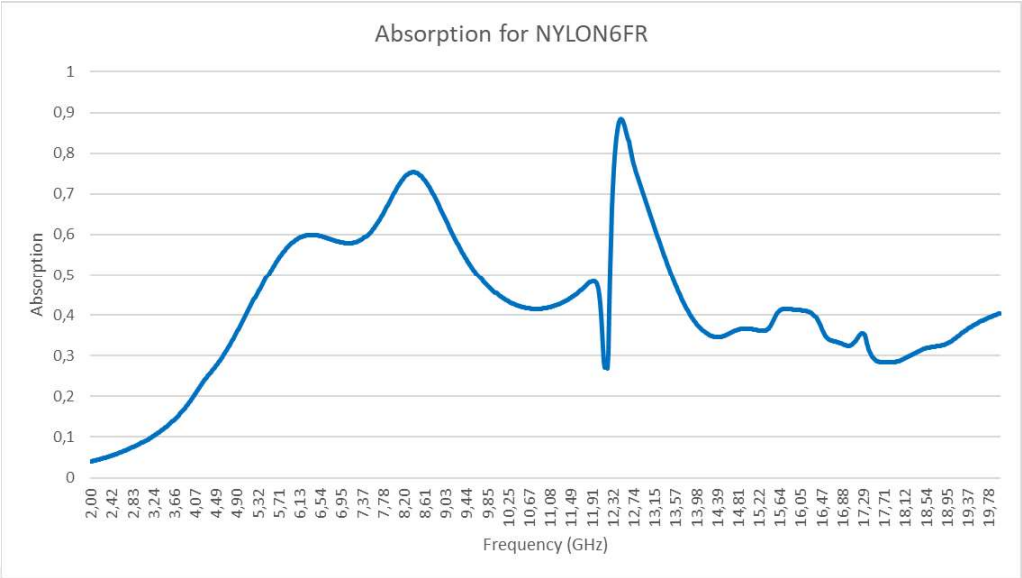

Figure 4.16 Absorption of MTM+FSS structure for NYLON6-FR

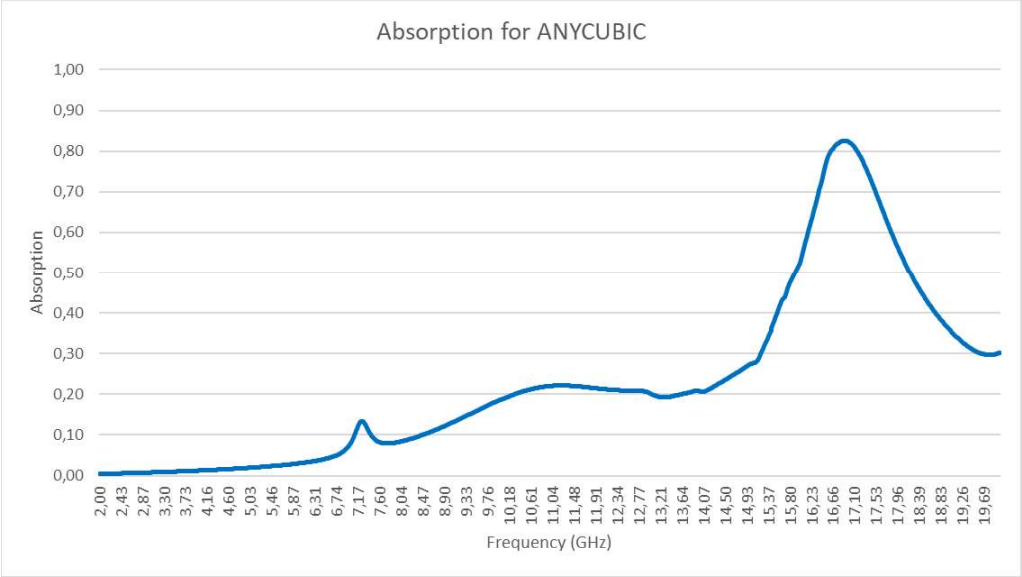

Figure 4.17 Absorption of MTM+FSS structure for ANYCUBIC Basic Resin

At 17 GHz there is an 82.5% absorption with this design of the structure when ANYCUBIC Basic Resin is used as a dielectric substrate.

4.1.2 Antenna Ground Plane Multilayer FSS Studies

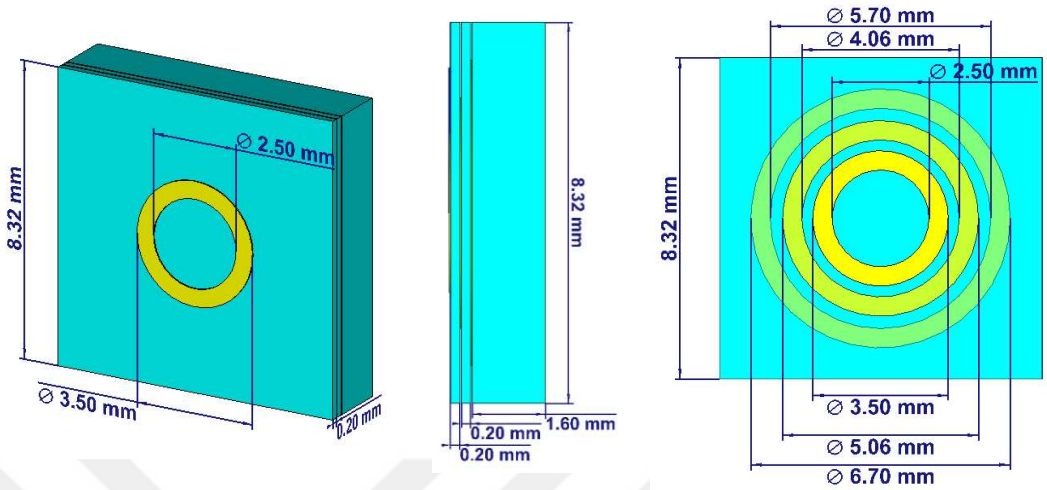

Figure 4.18 Multilayered FSS Structure dimensions and different oriented views

For the second case of reducing RCS by replacing the ground plane with an FSS structure backed with electromagnetic absorber foam. The designed FSS structure was simulated in an electromagnetic simulation program (CST Microwave Studio) and the scattering parameters were obtained with the waveguide ports connected to the parts facing the front and back sides of the structure. The obtained reflection and transmission graphs are given below.

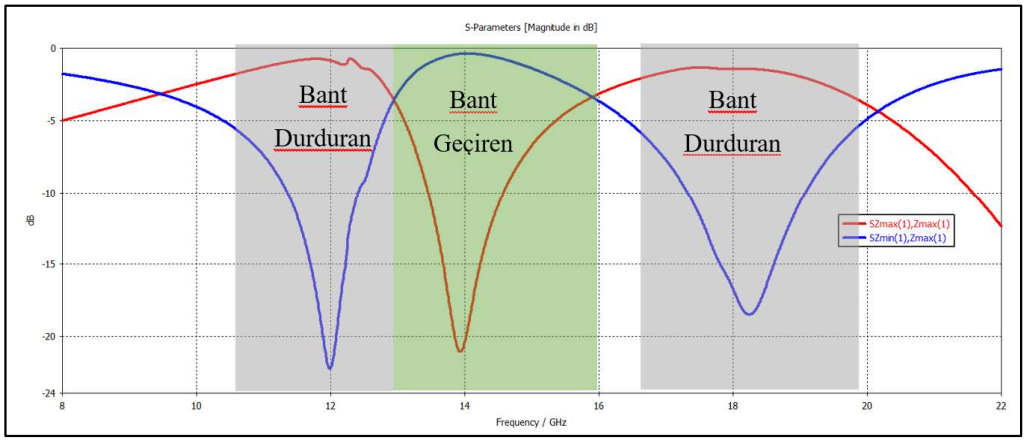

Figure 4.19 Reflection and Transmission graphs

In the graphs given in Figure 4.19, the graphs shown in red color indicate the reflection (S11) while the graph shown in blue color refers to the transmission (S21). When the

transmission and reflection graphs are examined, reflections close to 0 dB mean high reflection while lower magnitude values mean low reflections. Similarly, the transmission is high when the magnitude values are close to 0 dB and it is low if the magnitude has lower values. When these approaches are considered, it can be said that the design acts as a band-stop filter at the regions centered at f=12 GHz and f=18 GHz and there is a band-pass filtering property at the region centered at f=14 GHz. In other words, the designed structure can easily be used as a metallic ground plane for a dual-band antenna operating at 12 and 18 GHz. For this purpose, a dual-band dipole antenna working at the mentioned frequencies was developed. The shape and the detailed dimensions of the designed antenna are given in the following figure.

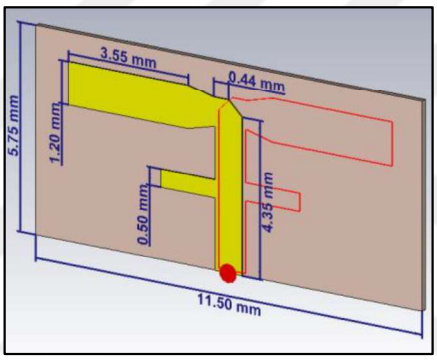

Figure 4.20 Dual-band dipole antenna structure

The return loss graph for the designed antenna is given in Figure 4.20. As seen in the figure, the designed antenna in Figure 4.21 has a good return loss behavior at f=12 GHz and f=18 GHz.

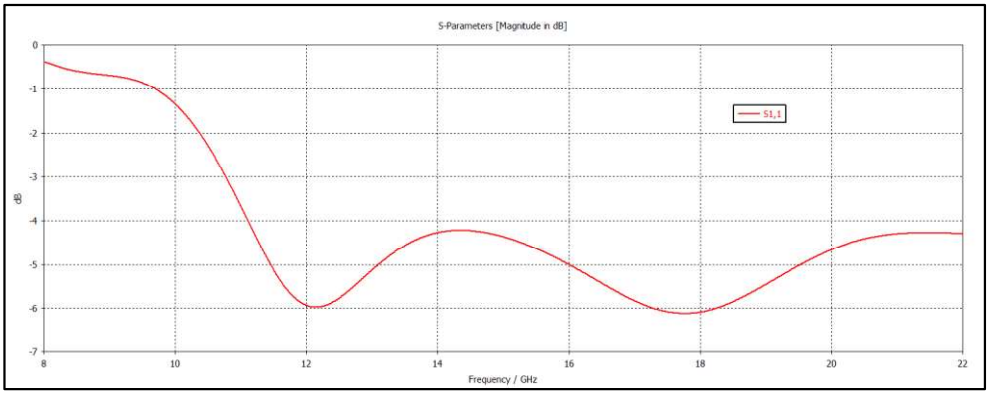

Figure 4.21 Return loss graph of the designed dual-band dipole antenna.

Far-field radiation patterns of the designed antenna are given in the following figure for the frequency points of f=12 GHz, f=14 GHz, and f=16 GHz.

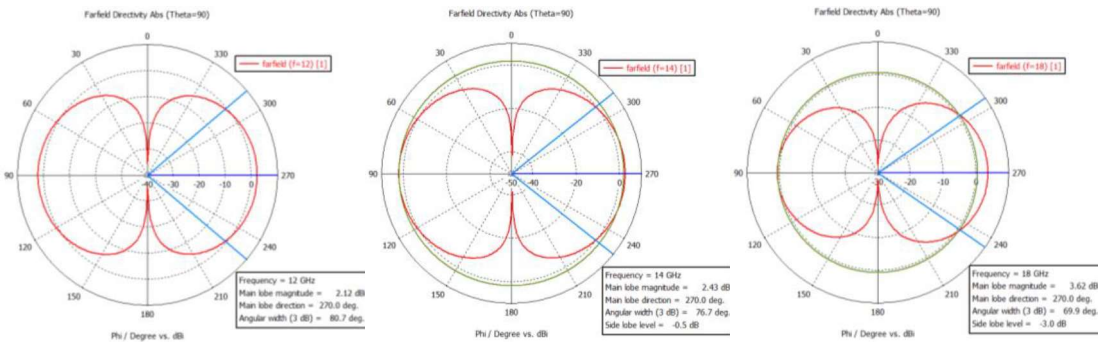

Figure 4.22 Far-field radiation patterns

As the reflective ground plane of the designed antenna structure, both a metallic plate and a periodic structure consisting of the FSS structures were used (Figure 4.23).

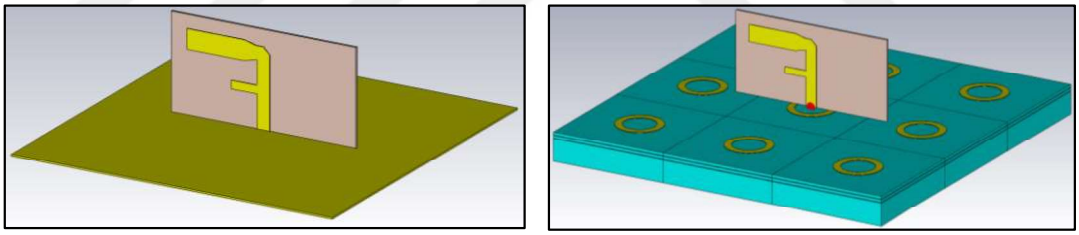

(a) (b)

Figure 4.23 The use of Metallic (a) and FSS (b) ground planes

The most important condition here is that the FSS structure must behave similarly with the metallic ground plane at the operation frequencies of the dual-band antenna and it does not affect nor alter the antenna performance. This can be examined by controlling the far-field radiation pattern as given in the following figure.

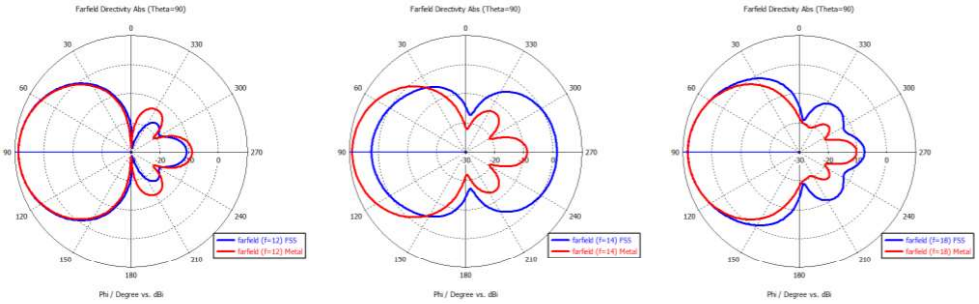

(a) (b) (c)

Figure 4.24 Far-field radiation patterns for the metallic ground and FSS-based ground plane for f=12 GHz (a), f=14 GHz (b), and f=18 GHz

When the far-field radiation behaviors are examined, it is seen that the FSS structure acts as a band-stop filter and exhibits a behavior very close to a metallic ground plane at f=12 GHz and f=18 GHz. On the other hand, the back lobe of the antenna is quite high at f=14 GHz where the FSS structure is intended to be used as a band-pass filter. Some important antenna parameters obtained by the use of metallic and FSS-based ground planes are tabulated below in Table 6. When the values given in the table are examined, it is seen that the FSS structure does not affect the antenna gain when it is used as the band-stop filter compared to the metallic ground plane while it reduced the back lobe more at the lower frequency point. In addition, one can see that the FSS structure increased the back lobe at f=14 GHz where the structure was used as the band-pass filter as if there is no ground plane at the back of the antenna.

Table 4.1 Antenna parameters for the use of FSS and Metallic ground plane

Frequency (f- GHz)	Antenna Gain (dB)		Back Lobe (dB)		Beam Width	
	FSS	Metal	FSS	Metal	FSS	Metal
12	8.62	8.65	-19.6	-17.7	60.7º	58.8
14	2.29	8.9	-1.0	-17.8	71.3º	55.3
18	8.12	8.17	-15.7	-18.5	61.7º	59.9

In order to test the ability of the study to reduce the radar cross-section constituting the main goal of the study, an RF absorber foam structure was placed at the back of the FSS ground plane structure. In this way, electromagnetic signals passing through the FSS structure will be absorbed by the foam materials. In this way, the RCS values will be decreased at all frequency points except for the ones where the antenna is operating. The shape of the structure used to simulate RCS is given in Figure 4.25.

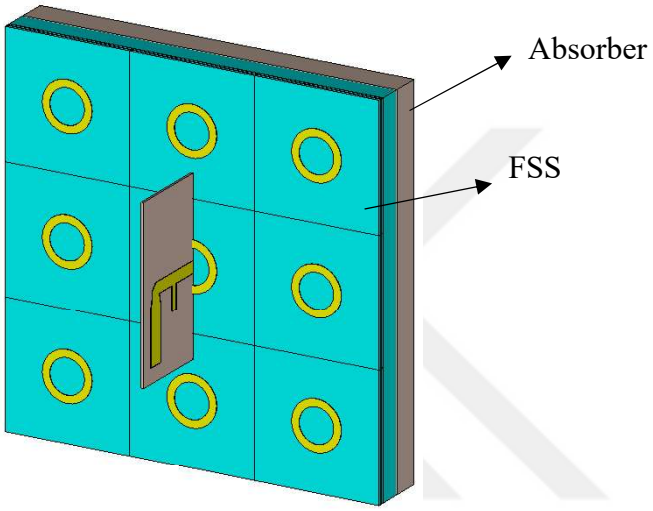

Figure 4.25 RCS simulation image by the addition of radar absorbing foam at the back of FSS periodic structure.

The simulation results for the radar cross-section were obtained as in Figure 4.26. It is clearly seen that RCS values are decreased significantly compared to the metallic ground plane version. In addition, the RCS value decreased significantly in the region where the FSS structure acts as a band-pass filter.

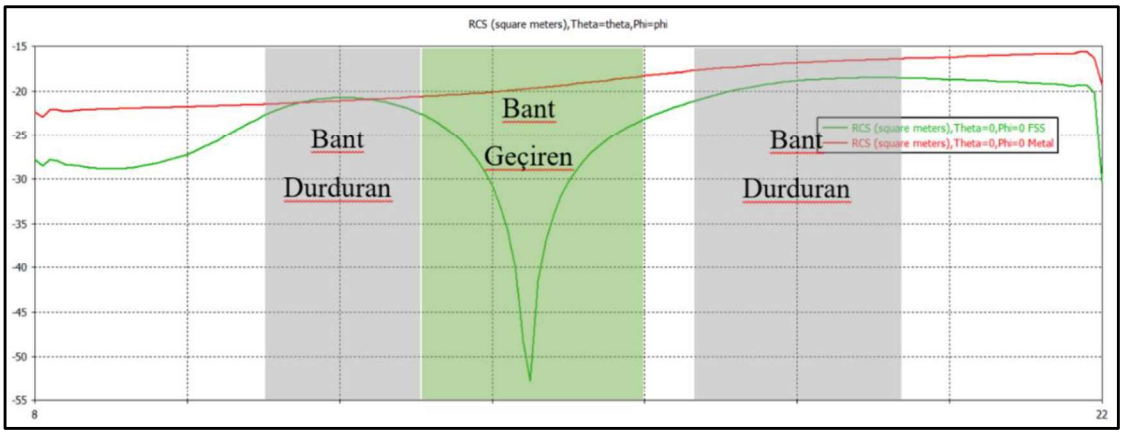

Figure 4.26 Radar Cross-section Graph obtained when FSS-based and Metallic Ground Planes are used.

4.1.3 Actual Multilayered FSS Manufactured for Antenna Ground Plane

Tests and simulations of multilayered FSS structures are conducted with different 3D-printed materials. If it was possible, the model shown in Figure 4.18 in the previous section 4.1.2 was going to be fabricated, because good results were acquired from study simulations. For the production phase, 0.2 mm thickness in the study was a very tight dimension to be produced by 3D printers in hand. Therefore, the structure thicknesses of layers had to be changed due to difficulties during the 3D printing manufacturing process. Therefore, the new dimensions were selected as shown in Figure 2.10. In order to ease the production phase, the substrate thickness values increased to 1.25 mm. In addition, the placement of the rings was changed so that they are arranged as Large, Medium, Small (LMS) and Small, Medium, Large (SML), and then the results were obtained for both cases numerically as well as experimentally. In the figure below, the LMS arrangement is illustrated for EM waveguide tests.

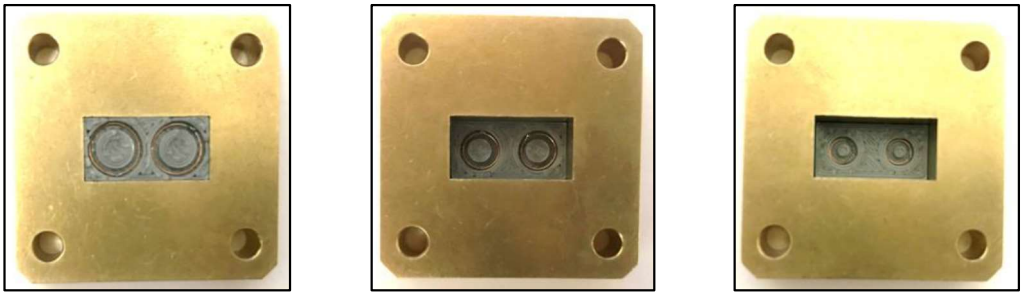

Large Groove Layer Medium Groove Layer Small Groove Layer

Figure 4.27 Multilayered FSS Test Specimen Installed on Sample Holder for EM Test

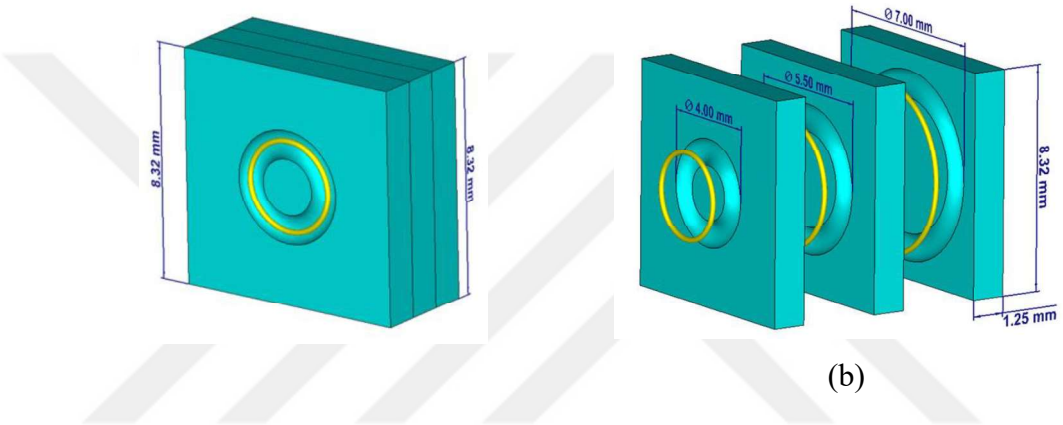

Figure 4.28 Increased substrate thickness and the placement of the rings according to their sizes (SML) (Assembly (a) and Exploded (b)).

3 different size copper rings were fabricated with copper wires that have the same cross-sectional diameter. The rings' inner diameters vary. Soldered the two ends together after giving them a round shape. The excessive solder is cleaned up as best as possible. But there are still some impurities in fabricating the copper rings. These tiny little human-made errors cause some inaccurate test results when correlating to simulation results.

The dimensions are illustrated in Figure 2.10 in section 2.1 under the title of fabrication processes of copper rings. And fabricated copper rings are also presented in Figure 2.1. The table below illustrates the sizes of the copper rings that are used for this study.

Table 4.2 Copper ring size information

	Cross-sectional diameter of wire	Inner diameter of rings
Small Ring	0.2 mm	3 mm
Medium Ring	0.2 mm	4.5 mm
Large Ring	0.2 mm	6 mm

Five different substrate materials that are produced by using 3D printers were tested. The first sample is ANYCUBIC titled substrate and its simulation and measurement results are given below.

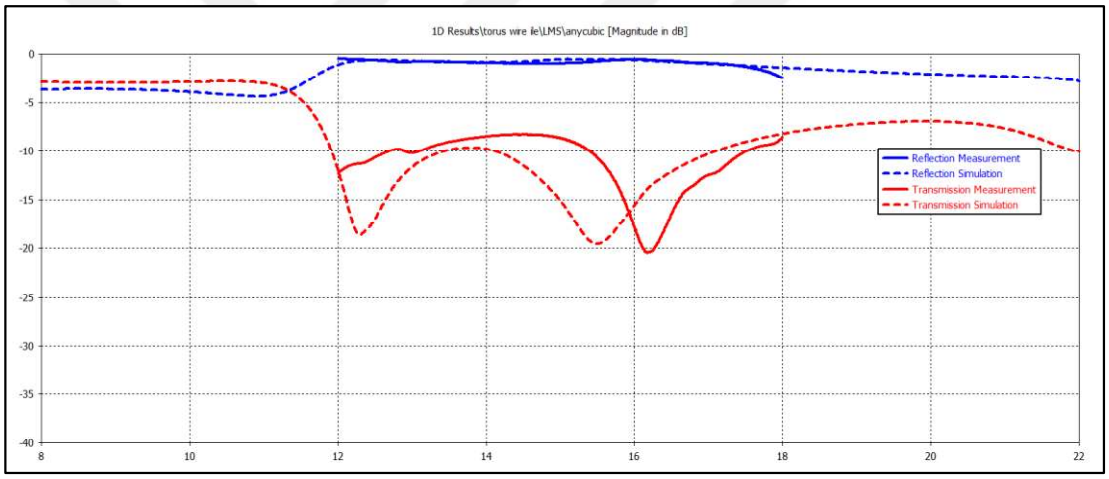

Figure 4.29 Reflection and Transmission results from the Simulation and Experimental tests of the structure with ANYCUBIC substrate (LMS)

ANYCUBIC Basic Resin layers stacked from large to small size grooves (LMS orientation). Large rings were facing incoming EM waves during the waveguide test. As seen in Figure 4.29 simulation results (dashed lines) and test results (solid lines) are displaying similar behavior. In simulation results, there is a strong transmission near 12.5 GHz and 15.5 GHz. And in test results, the good transmission behavior in 12 GHz – 16 GHz bandwidth. Reflection values are close to 0, meaning that almost no reflection throughout the 12-18 GHz frequency band.

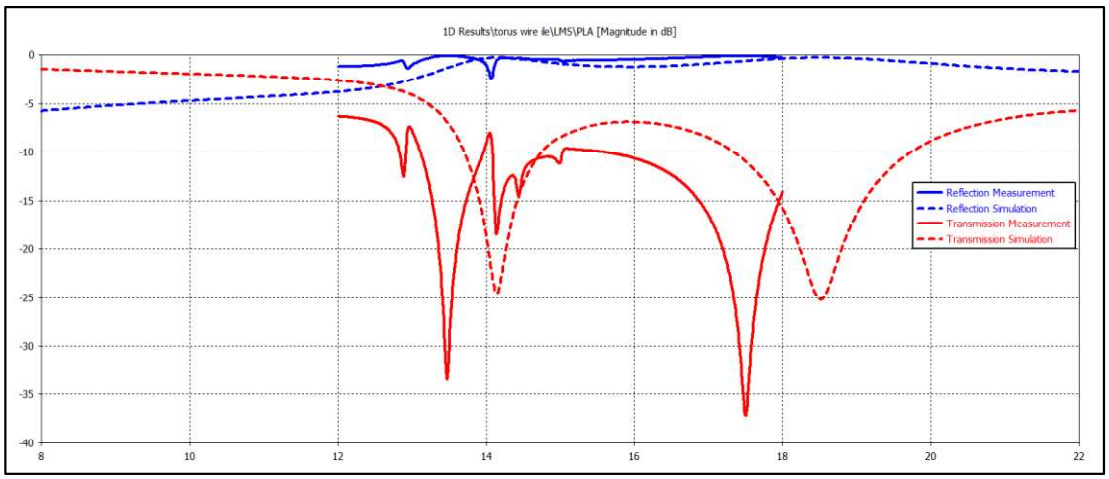

Figure 4.30 Reflection and Transmission results from the Simulation and Experimental tests of the structure with PLA substrate (LMS)

PLA layers were also stacked as LMS orientation. So that large rings were facing incoming EM waves during the waveguide test. As seen in Figure 4.30 simulation results (dashed lines) and test results (solid lines) are displaying similar but shifted behavior in the figure above. In simulation results, there is a good transmission near 14 GHz and 18.5 GHz. In test results, these transmission values are at 13.5 GHz to 17.5 GHz. Reflection values are close to 0, meaning that almost no reflection throughout the whole frequency band.

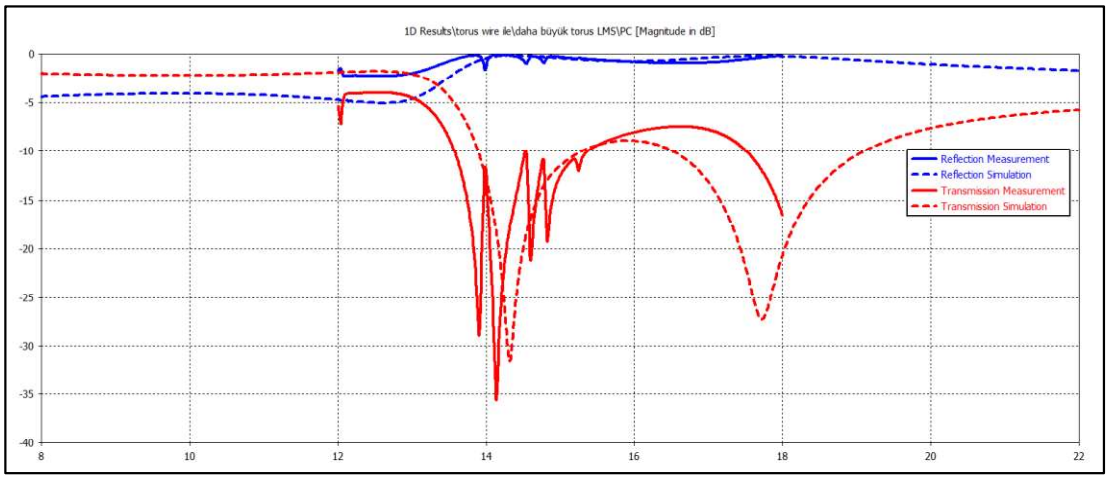

Figure 4.31 Reflection and Transmission results from the Simulation and Experimental tests of the structure with PC substrate (LMS)

Polycarbonate layers stacked from large to small size grooves (LMS orientation). Large rings were facing incoming EM waves during the waveguide test. As seen in Figure 4.31 simulation results (dashed lines) and test results (solid lines) are displaying similar behavior in the figure above. In both simulation and test results, there is a strong transmission near 14 and 18 GHz. And reflection values are close to 0, meaning that almost no reflection throughout the whole frequency band.

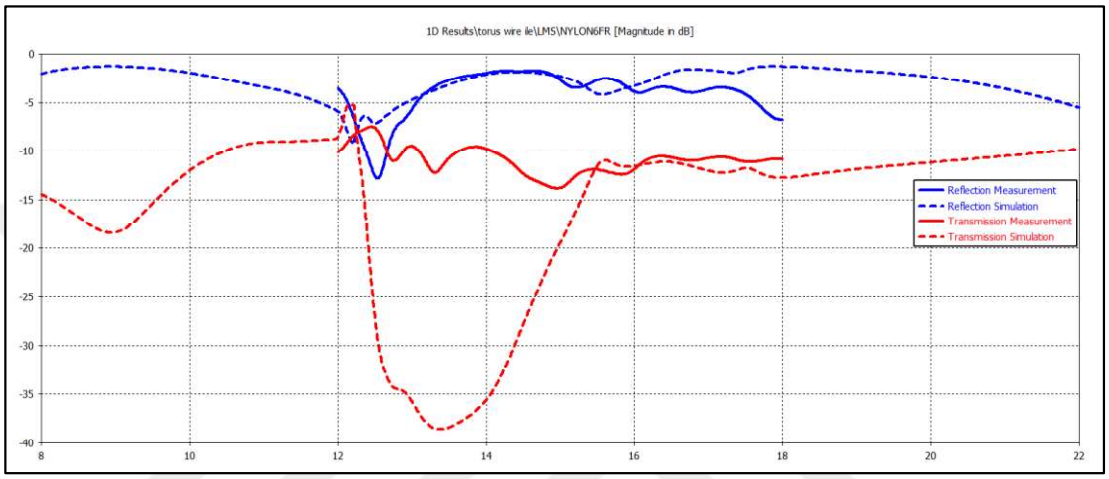

Figure 4.32 Reflection and Transmission results from the Simulation and Experimental tests of the structure with NYLON6FR substrate (LMS)

As seen in Figure 4.32 again LMS orientation of the multilayered structure is used for simulations and tests. NYLON6 FR material is a polymer that is 3D-printed, but it shows similar behavior as conductive layers rather than dielectric layers, especially at around 12.5GHz. This type of behavior indicates that the reflective and transmission properties are strongly related to the operating frequency of the system. For transmission properties according to the figure above, test (solid line) and simulation (dashed line) results are not even close. When it comes to reflection results, the values are relatively close to each other. This is an interesting 3D printing material that requires more research related to electromagnetic studies.

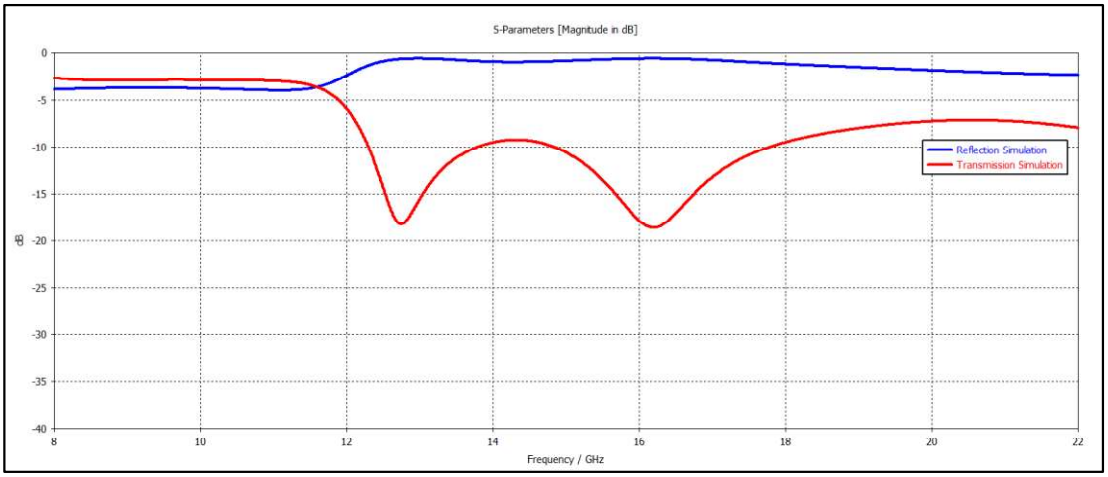

Figure 4.33 Reflection and Transmission results from the Simulation tests of the structure with ULTEM substrate (LMS)

Because of the production problems and tight tolerances in our design, only the samples suitable for electromagnetic characterization through waveguide setup can be produced for ULTEM substrates. Therefore, only the simulation results were obtained in the above graph (Figure 4.33).

When the rings are located backward, that is the small one facing to the incident wave while the large one is placed at the back (SML), the following simulation and experimental results were obtained. In Figure 4.34, the reflection and transmission results of the structure can be seen both experimentally and analytically using ANYCUBIC substrate in the order of SML. The experimental results are shown in red color and have a good agreement with the simulation results. The experimental data cover the frequency band of 12-18 GHz while the simulation was run between 8-22 GHz. Although there is a slight shift in the curves, overall behavior is similar for ANYCUBIC substrate. It should be noted that the complex electromagnetic permittivity and permeability values obtained for experimental data were used using data fitting in order to simulate the remaining frequency points. Manufacturing errors along with non-perfect laboratory equipment might be the cause of slight shift in the data.

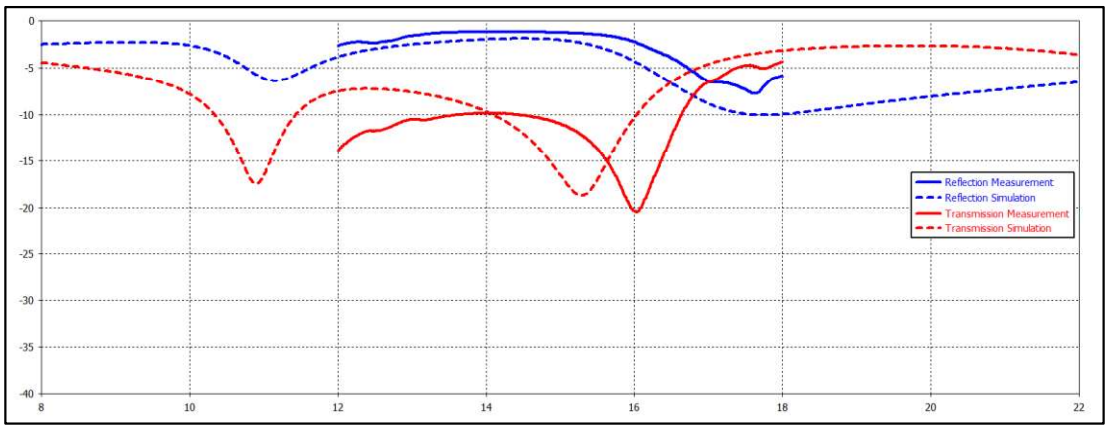

Figure 4.34 Reflection and Transmission results from the Simulation (Dashed Lines) and Experimental (Solid Lines) tests of the structure with ANYCUBIC substrate (SML)

In the other case, substrate material was changed with PLA and the following reflection and transmission behaviors were obtained both experimentally and analytically. The resonance obtained at high frequencies (at around 18 GHz) is very close to each other while there is a sharp magnitude decrease at around 13 GHz. Overall, the structure still provides a band-stop behavior at the desired frequency points which is the essence of the study.

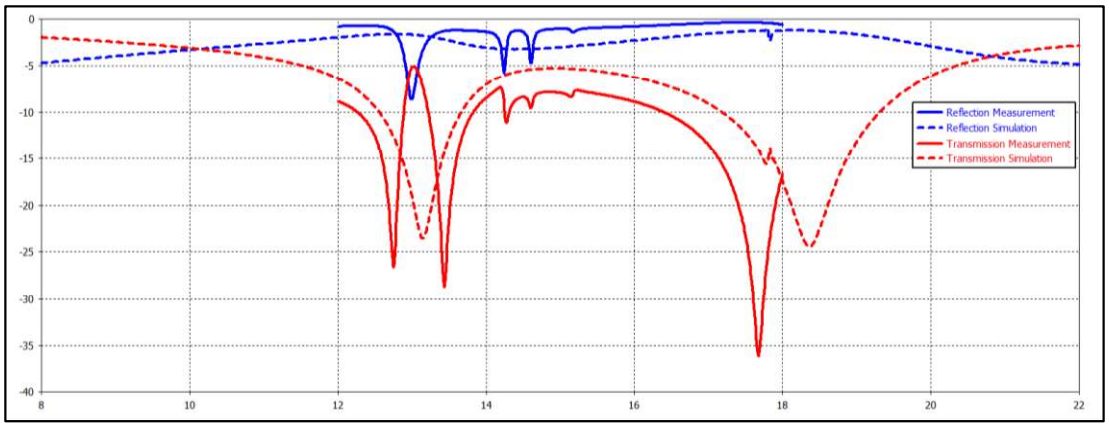

Figure 4.35 Reflection and Transmission results from the Simulation (Dashed Lines) and Experimental (Solid Lines) tests of the structure with PLA substrate (SML)

In the next part, PC substrate was used for SML arrangement and the reflection and transmission curves were obtained. The following figure shows the experimental (solid lines) and analytical (dashed lines) reflection and transmission behaviors. One can observed that the band-stop behavior can be observed at two distinct frequencies. Since

the experimental tests were carried out between 12-18 GHz. There is slight frequency shift in the curves due to manufacturing errors and non-perfect lab conditions and equipments which is also the case for all tests.

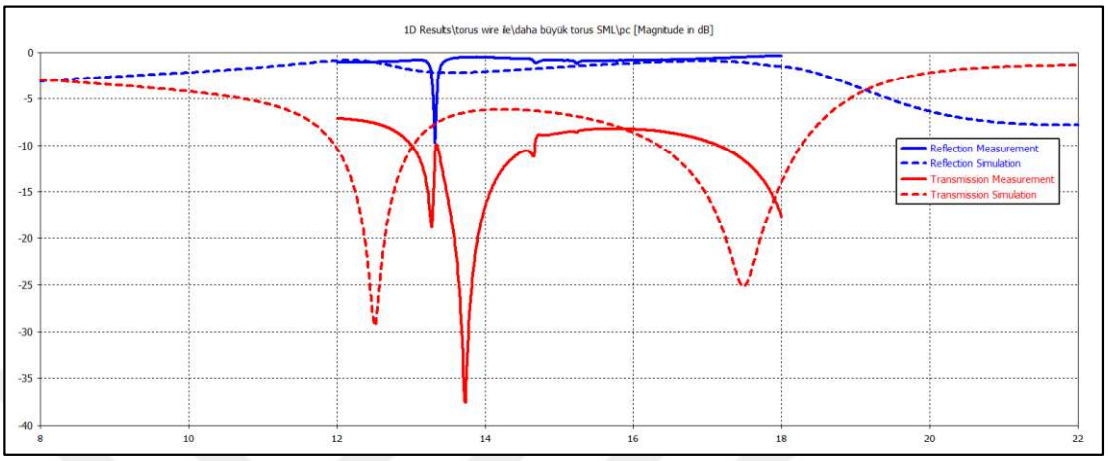

Figure 4.36 Reflection and Transmission results from the Simulation (Dashed Lines) and Experimental (Solid Lines) tests of the structure with PC substrate (SML)

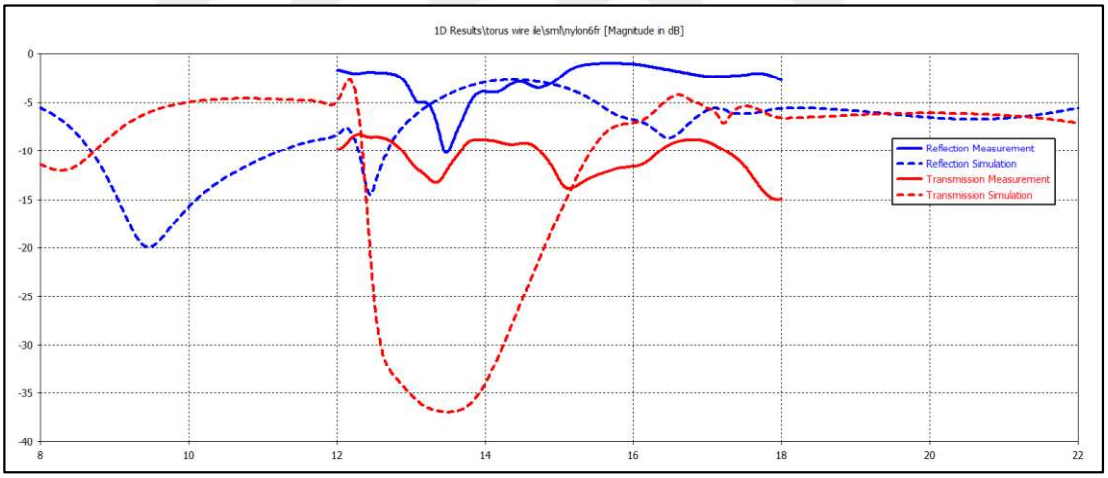

Figure 4.37 Reflection and Transmission results from the Simulation and Experimental tests of the structure with NYLON6FR substrate (SML)

As in the SML case, no experimental study can be carried out for the ULTEM substrate sample. The simulation study was conducted and the reflection and transmission responses are given in the figure below (Figure 4.38).

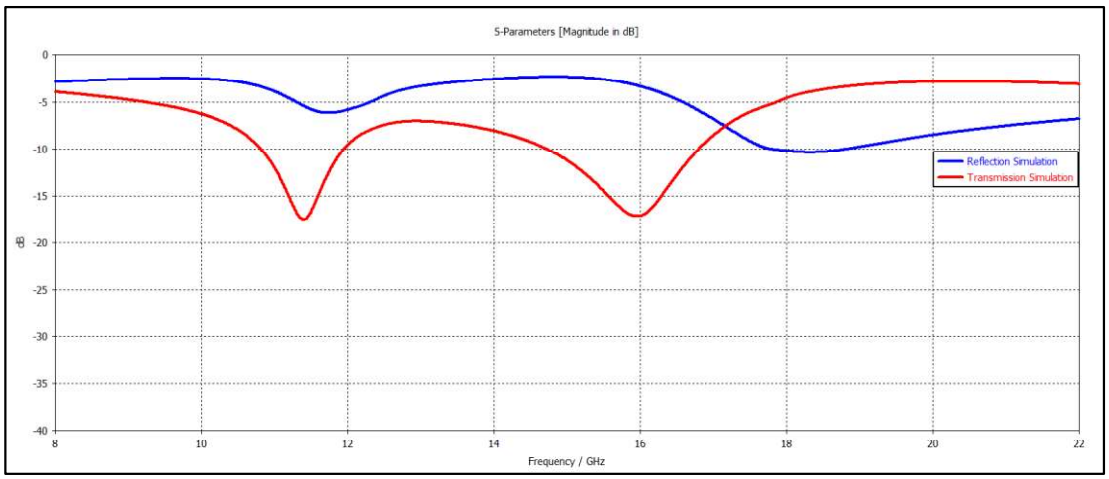

Figure 4.38 Reflection and Transmission results from the Simulation tests of the structure with ULTEM substrate (SML)

4.2 Mechanical Tensile Test Results

According to ASTM D638 standards, Type V is usually used for exceptional cases, for example, thermal and environmental stability tests or it can also be used if there is only a limited amount of material available. The thickness of the specimens shall be defined as 4 mm or less for evaluations.

In this study, the amount of material that are obtained was not sufficient, as a result, we ended up selecting Type V from ASTM D638 tensile test standards with a thickness of 3 mm. Five test specimens were manufactured for each 3D printing material and mechanical strength characteristics are obtained by tensile testing. It is unfortunate that contacting extensometers were not used due to the fact that the specimen standard sizes were very small. And strain gages were not available. Therefore, the strain values were not measured during the tensile tests. However, the Extension-vs-Force plots are obtained for each specimen. Through these plots, the ultimate tensile strengths of four different materials of 3D-printed samples are measured. And that will give an idea of 3D-printed materials' structural endurance.

It can be said that test results show significant differences among each other in terms of strength that different materials can withstand. The average ultimate tensile strength values for each 3D-printed material are tabulated (in Table 4.3-4.6) along with the results. Each and every test specimen dimension are measured and recorded. The measured gage dimensions are entered into the Universal Testing System's computer before the tests are performed. With these dimensions, the cross-sectional areas of the gage section can also be obtained for hand calculations. Since extensometers or strain gages were not available for tensile tests, it is not possible to calculate Young's modulus, Poisson's ratio, and yield strength accurately. But roughly, estimated values for 0.2% Yield Strengths, Young's Moduli, Axial Stresses, and Strains can be computed and compared. However, the obtained ultimate strengths of all materials will give adequate information about these four different materials' structural behavior.

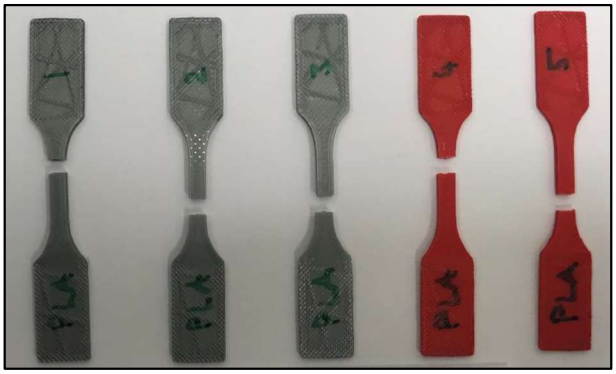

a-) PLA

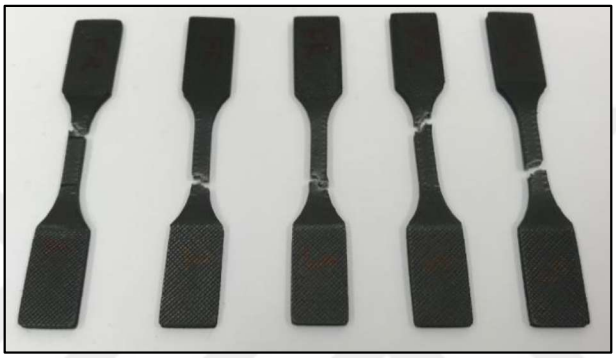

b-) NYLON6-FR

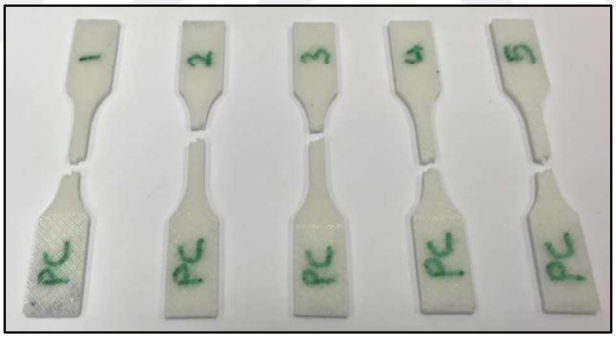

c-) Polycarbonate

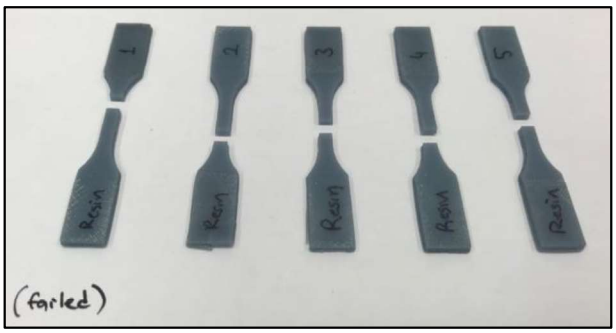

d-) ANYCUBIC Basic Resin

Figure 4.39 TYPE V ASTM D638 Broken Specimens after Tensile Testing

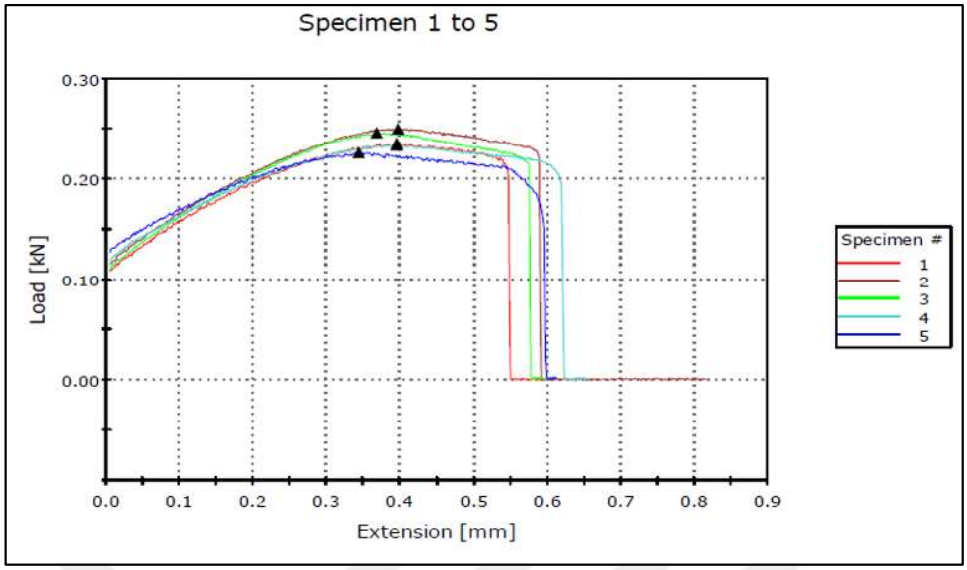

Figure 4.40 PLA Tensile Test Strength Results

The speed rate of pulling apart in tensile tests for all specimens was 1mm/min. Load – vs- Extension plots for PLA are obtained after tests shown in Figure 4.40. Test results are also obtained and strain values are calculated by dividing extension by the initial length of the specimens with the formula given as $\Delta L/L_0$. Stress values ($\sigma_{tensile}$) are also calculated by dividing the load by the cross-section area of the gage section of the specimens given in the equation as F/A_0. Below in Figure 4.41, Stress-Strain curves of PLA test specimens are presented.

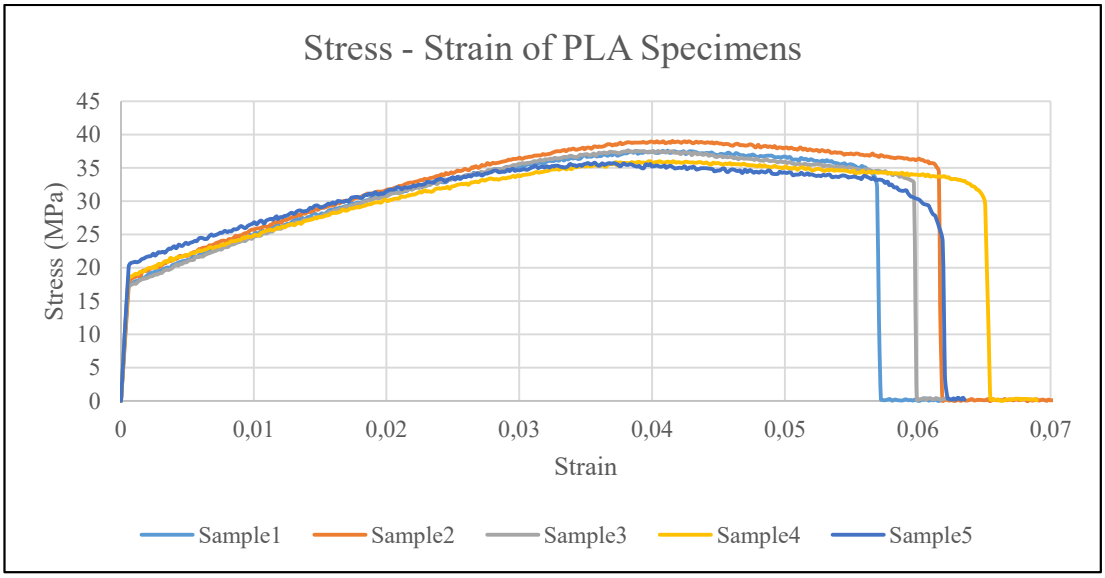

Figure 4.41 PLA Stress-Strain Curve

Table 4.3 PLA Calculated Yield Strength and Elastic Modulus

	TENSILE TEST	Sample 1	Sample 2	Sample 3	Sample 4	Sample 5	**Average**	**Min.**	**Max.**
PLA	Thickness (mm)	1.92	1.91	1.95	1.95	1.9	1.926	1.9	1.95
	Gage width (mm)	3.26	3.35	3.35	3.33	3.33	3.324	3.26	3.35
	Gage Length (mm)	9.6	9.56	9.63	9.5	9.62	9.582	9.5	9.63
	Ultimate Tensile Strength (MPa)	**37.62**	**39.05**	**37.63**	**36.02**	**35.78**	**37.22**	**35.78**	**39.05**
	Maximum Force (N)	**235.47**	**249.85**	**245.79**	**233.89**	**226.41**	**238.282**	**226.41**	**249.85**
	Axial Stress (MPa)	17.37672	18.14995	16.89379	18.4056	20.14581	18.194374	16.89379	20.14581
	Strain	0.000566667	0.000632	0.000512	0.000572	0.000586279	0.000573789	0.000512	0.000632
	Yield Strength (MPa) (0.2%)	19.4	20.07	18.95	19.94	21.83	20.038	18.95	21.83
	Elastic Modulus (GPa)	30.665	28.718	32.996	32.178	34.362	31.784	28.718	34.362

For PLA tensile test specimens, the dimensions of gage thickness, width, and length are measured. These measured data are entered in UTS software and as a result after tensile tests, ultimate tensile strength (MPa) and maximum force (N) are obtained for each specimen individually. In addition, these measured data are used to do hand calculations to obtain “inaccurate but close” values for yield strength and elastic modulus of PLA.

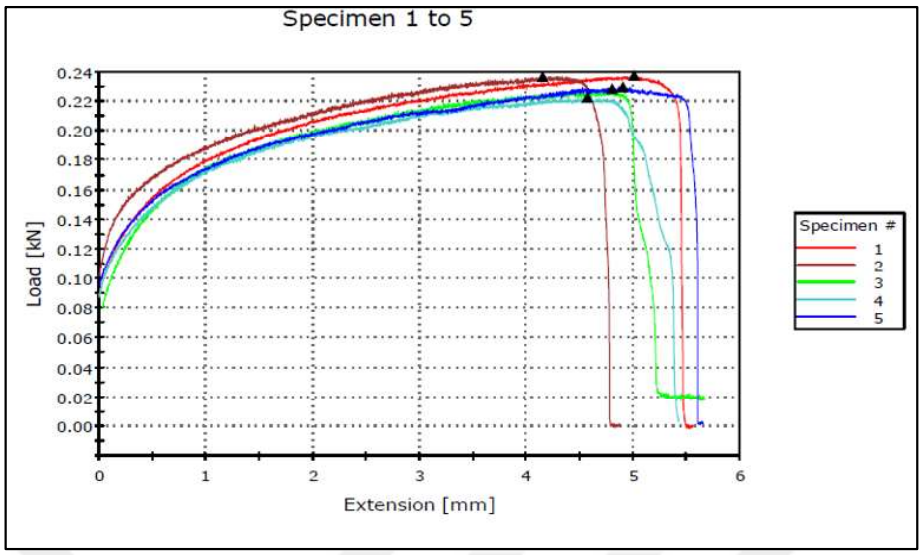

Figure 4.42 NYLON6-FR Tensile Test Strength Result

Load –vs- Extension plots for NYLON6-FR are obtained from tensile tests, shown in Figure 4.42. Test results are also obtained and strain values are calculated by $\Delta L/L_0$. Stress values ($\sigma_{tensile}$) are also calculated by F/A_0. Below in Figure 4.43, Stress-Strain curves of NYLON6-FR test specimens are presented. The strain rate range of the test specimens is displayed between 0.5-0.6. In Table 4.4, the average ultimate tensile strength and average maximum force values are illustrated as 34.9 MPa and 231.03 N respectively.

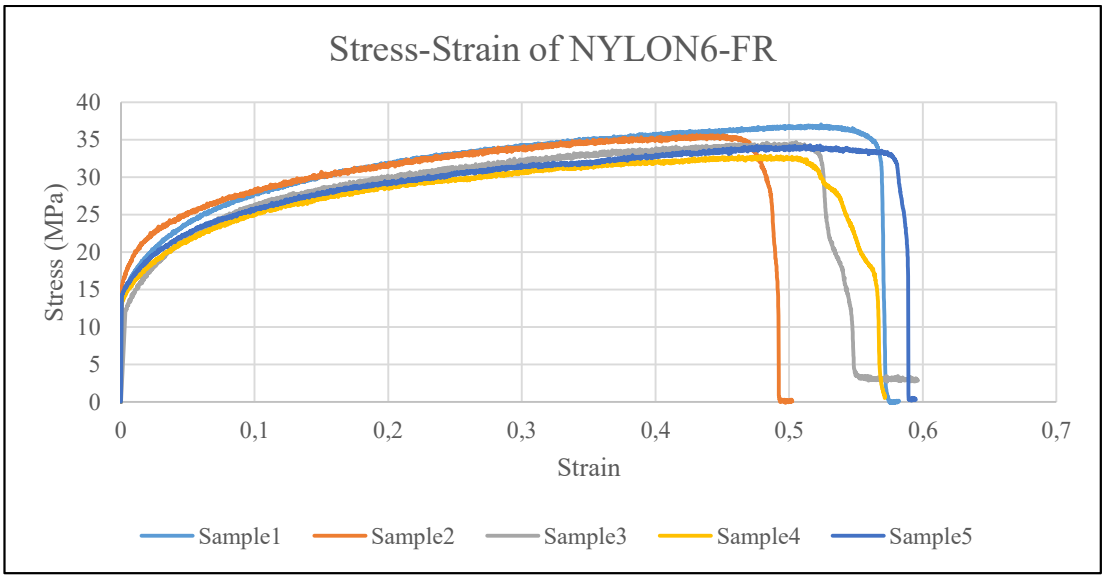

Figure 4.43 Stress-Strain Curve of NYLON6-FR

Table 4.4 NYLON6-FR Calculated Yield Strength and Elastic Modulus

	TENSILE TEST	Sample 1	Sample 2	Sample 3	Sample 4	Sample 5	Average	Min.	Max.
NYLON6 FR	Thickness (mm)	2.01	2.02	2	2.01	2.02	2.012	2	2.02
	Gage width (mm)	3.19	3.29	3.29	3.37	3.32	3.292	3.19	3.37
	Gage Length (mm)	9.55	9.7	9.5	9.48	9.5	9.546	9.48	9.7
	Ultimate Tensile Strength (MPa)	**37.05**	**35.61**	**34.72**	**32.87**	**34.26**	**34.902**	**32.87**	**37.05**
	Maximum Force (N)	**237.59**	**236.68**	**228.46**	**222.65**	**229.77**	**231.03**	**222.65**	**237.59**
	Axial Stress (MPa)	13.69045	15.32151	12.40658	12.97663	14.24375	14.058085	12.97663	15.32151
	Strain	0.00054555	0.000606186	0.00348	0.000375527	0.000781053	0.000577079	0.000375527	0.000781053
	Yield Strength (MPa) (0.2%)	14.9	16.58	13.28	14.07	15.22	15.1925	14.07	16.58
	Elastic Modulus (GPa)	25.095	25.275	3.565109195	34.556	18.237	25.791	18.237	34.556

As for NYLON6 FR, sample 3 test results are not taken into consideration for yield strength and Young's modulus calculations. The calculated values for this specific specimen were far off from the expected values and they were affecting the average and the minimum values of overall specimens. But the ultimate tensile strength and maximum force data that are received from the test results are correct and accurate. The yield strength and elastic modulus values are not accurate, they will only give an idea about their mechanical behavior roughly. However, these calculated elastic modulus and yield strength shown in Table 4.4 should not be taken as references. In addition to that, this material shows stronger characteristics than ANYCUBIC.

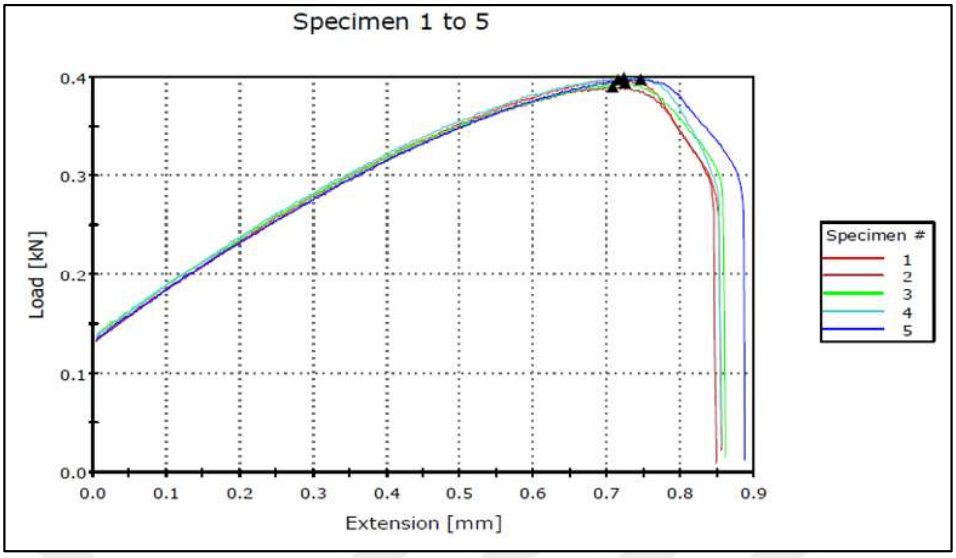

Figure 4.44 PC Tensile Test Strength Result

Load –vs- Extension plots for POLYCARBONATE are obtained from tensile tests, shown in Figure 4.44. Test results are also obtained and strain values are calculated by $\Delta L/L_0$. Stress values ($\sigma_{tensile}$) are also calculated by F/A_0. Below in Figure 4.45, Stress-Strain curves of POLYCARBONATE test specimens are presented. The strain rate range of the test specimens are displayed between 0.85-0.9. In Table 4.5, the average ultimate tensile strength and average maximum force values are illustrated as 57.5 MPa and 395.36 N respectively.

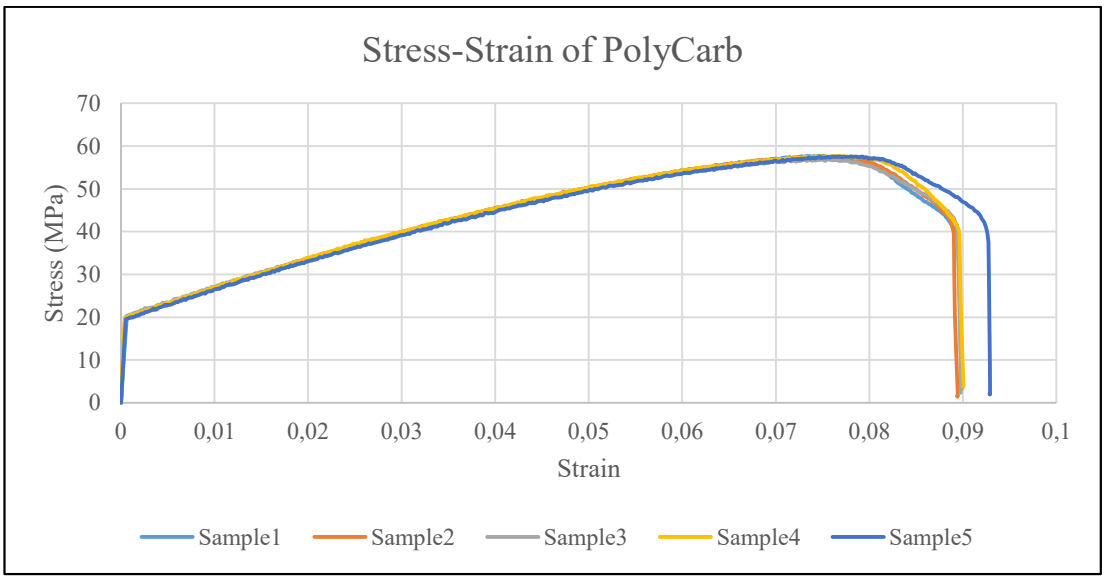

Figure 4.45 Stress-Strain Curve of PC

Table 4.5 PC Calculated Yield Strength and Elastic Modulus

	TENSILE TEST	Sample 1	Sample 2	Sample 3	Sample 4	Sample 5	Average	Min.	Max.
PC	Thickness (mm)	2.17	2.14	2.17	2.16	2.17	2.162	2.14	2.17
	Gage width (mm)	3.17	3.17	3.18	3.2	3.18	3.18	3.17	3.2
	Gage Length (mm)	9.51	9.48	9.58	9.5	9.54	9.522	9.48	9.58
	Ultimate Tensile Strength (MPa)	**57.71**	**57.43**	**57.08**	**57.71**	**57.59**	**57.504**	**57.08**	**57.71**
	Maximum Force (N)	**397**	**389.62**	**393.86**	**398.9**	**397.44**	**395.364**	**389.62**	**398.9**
	Axial Stress (MPa)	19.77193	19.58191	20.1455	19.75813	19.44399	19.740292	19.44399	20.1455
	Strain	0.000622503	0.000414557	0.000538622	0.000407368	0.000530398	0.00050269	0.000407368	0.000622503
	Yield Strength (MPa) (0.2%)	21.5	23.8	22.15	21.56	21.2	22.042	21.2	23.8
	Elastic Modulus (GPa)	31.762	47.236	37.402	48.502	36.659	40.312	31.762	48.502

For POLYCARBONATE tensile test specimens, the dimensions of gage thickness, width, and length are measured as well. Measurements are entered into the UTS computer and as a result after tensile tests, ultimate tensile strength (MPa) and maximum force (N) are obtained for each specimen individually. In addition, these measured data are used to do hand calculations to obtain values for yield strength and elastic modulus of POLYCARBONATE. Even though the yield strength and elastic modulus results are inaccurate, these calculations will give an idea about their mechanical properties. However, these calculated elastic modulus and yield strength shown in Table 4.5 should not be taken as references.

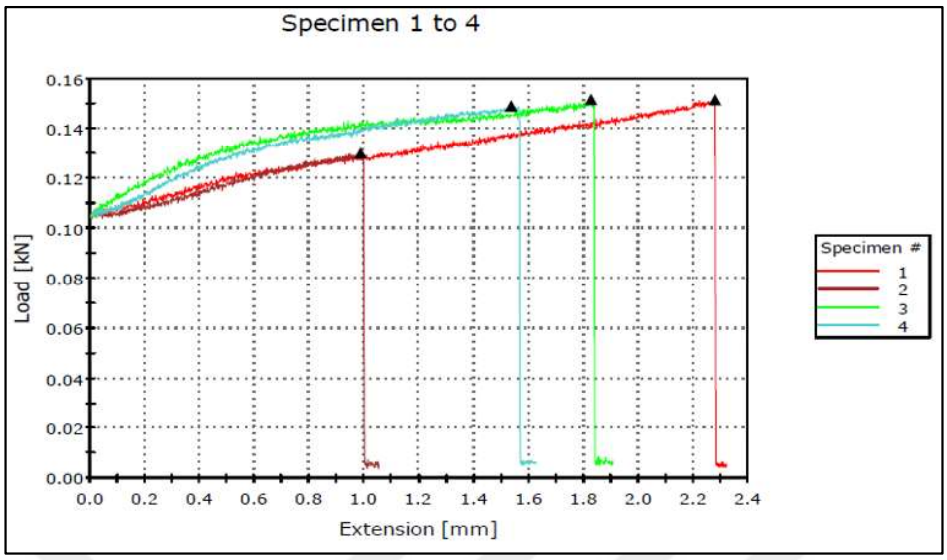

Figure 4.46 ANYCUBIC Basic Resin Tensile Test Strength Result

Load -vs- Extension plots for ANYCUBIC Basic Resin are obtained from tensile tests, shown in Figure 4.46. One of the test specimens was damaged by the test operator which is why only four specimens were tested. Below in Figure 4.47, Stress-Strain curves of ANYCUBIC Basic Resin test specimens are shown. Strain rates are really low and the strain range of the test specimens is displayed between 0.1-0.25. In Table 4.6, the average ultimate tensile strength and average maximum force values are displayed as 20.35 MPa and 145.57 N respectively.

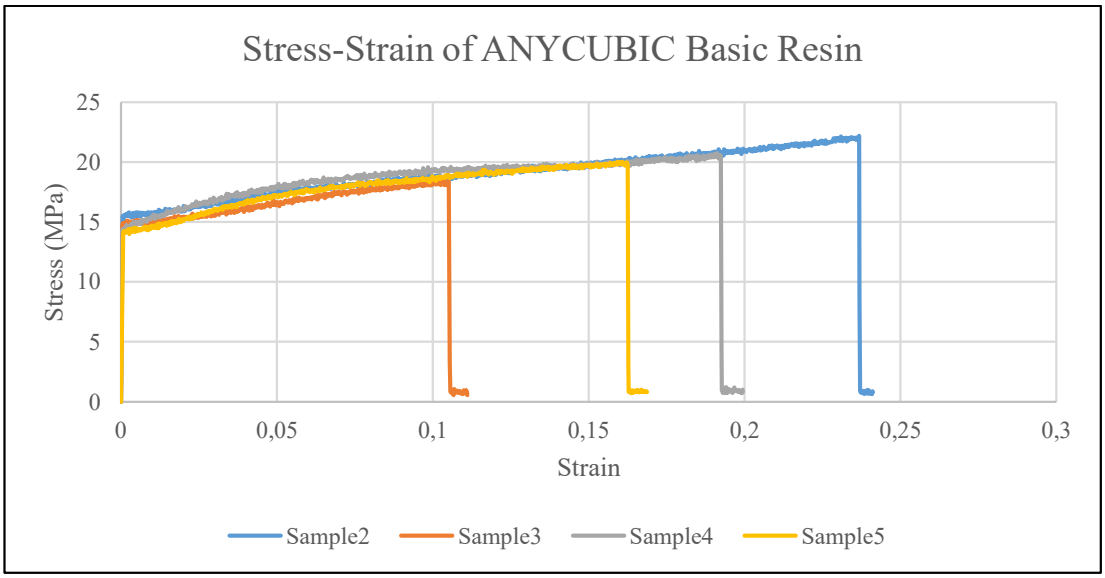

Figure 4.47 Stress-Strain Curve of ANYCUBIC Basic Resin

Table 4.6 ANYCUBIC Basic Resin Calculated Yield Strength and Elastic Modulus

	TENSILE TEST	Sample 1	Sample 2	Sample 3	Sample 4	Sample 5	**Average**	**Min.**	**Max.**
ANYCUBIC Basic Resin	Thickness (mm)	2.25	2.07	2.19	2.13	2.2	2.168	2.07	2.25
	Gage width (mm)	3.3	3.3	3.22	3.43	3.38	3.326	3.22	3.43
	Gage Length (mm)	9.53	9.62	9.48	9.55	9.63	9.562	9.48	9.63
	Ultimate Tensile Strength (MPa)	-	**22.18**	**18.45**	**20.75**	**20.04**	**20.355**	**18.45**	**22.18**
	Maximum Force (N)	-	**151.51**	**130.13**	**151.62**	**149**	**145.565**	**130.13**	**151.62**
	Axial Stress (MPa)	-	15.44949	14.74481	14.35177	14.14224	14.6720775	14.14224	15.44949
	Strain	-	0.000529106	0.000439873	0.000406283	0.000739356	0.000528655	0.000406283	0.000739356
	Yield Strength (MPa) (0.2%)	-	15.45	14.74	14.35	14.14	14.67	14.14	15.45
	Elastic Modulus (GPa)	-	29.199	33.521	35.3246	19.128	29.293	19.128	35.325

For ANYCUBIC Resin, the tensile test specimens were solidified by photo lights at a wavelength of 405 nm. In addition to that, the specimens required a post-curing as well. But the equipment which was necessary for post-curing was not present. So that post-curing is handled at room temperature for more than 24 hours. Even though the specimen sizes were close to each other, the tensile test results were not as close. ANYCUBIC was the most brittle and weakest among all other 3D-printed materials in terms of mechanical strength.

CHAPTER 5

CONCLUSION

In conclusion, the idea of using metamaterials with frequency-selective surfaces worked well in the structure we designed in this study. Substrate samples are manufactured as 3D-printed parts. With FDM 3D printing method, four different filament materials are used to fabricate for EM and mechanical tensile tests, and one photo-curable liquid resin material is used to fabricate EM and tensile test specimens with SLA 3D printing method. For all test samples that are built with 3D printing filaments -/+45° raster angle orientation was selected due to their structural stability under loads.

EM di-electric substrate samples were built in a volume of 15.8 x 7.9 x 3 mm^3 and they were tested with a waveguide measurement system to obtain EM properties. EM Properties are characterized for each substrate, so ε and μ values are obtained.

Design assemblies for Radome Structures are created consisting of MTM, FSS and

3D-printed dielectric substrates on simulation tool. EM analyses are conducted on these different design assemblies. The max. EM Absorption is achieved at about 82.5% with ANYCUBIC, and 70% with ULTEM9085 FR. The best EM absorption characteristics order is ANYCUBIC > ULTEM9085FR> PC > PLA > NYLON6FR.

Multilayered FSS Structures as antenna back plates are fabricated. Waveguide EM tests are conducted, and test results are obtained. Computer simulations are completed. EM performance with LMS configuration can be shown as PLA > PC > ANYCUBIC > ULTEM9085FR > NYLON6FR. EM performance with SML configuration can be demonstrated as PC > PLA > ULTEM9085FR >ANYCUBIC > NYLON6FR.

Mechanical tensile tests are conducted for strength check and the highest ultimate tensile strength to the lowest order can be displayed as PC > PLA > NYLON6FR > ANYCUBIC. ULTEM 9085FR material is not sufficient to fabricate samples for

mechanical tensile tests. Therefore ULTEM 9085 FR was not taken into consideration for tensile tests.

Normally, an FSS structure built for a band-pass behavior allow signals at a certain frequency band while reflecting the rest of the signals in different frequencies. With the combination we suggested in this paper, high frequencies are absorbed with the help of a metamaterial split ring resonator structure placed on the other side of the assembly. This can be seen both from the absorption graphs and from the transmission/reflection graphs. It is obvious that absorbing signals rather than reflecting back fully will significantly reduce the radar cross-section of the structure. Finally, it can be said that this structure and approach can be used safely and easily particularly in antenna radomes to reduce RCS in various applications. The challenging part of this study will be the application of this structure on non-planar surfaces which will be the future study on this subject.

REFERENCES

[1] Lapedes, DN. Dictionary of scientific and technical terms. New York; Montreal: McGraw-Hill 1976: p.1634, A26. ISBN-13. 978-0070423138

[2] Vinoy KJ. Radar absorbing materials from theory to design and characterization. Boston: Kluwer Academic Publisher 1996: p. 1–16, p. 116–120, p. 135–138, p. 146–157. ISBN-13 : 978-1461380658

[3] Chin WS, Lee DG. Binary mixture rule for predicting the dielectric properties of unidirectional E-glass/epoxy composite. Compos Struct 2006; 74: p. 153-162.

[4] Lee, J.Y., An, J., Chua, C.K., "Fundamentals and applications of 3D printing for novel materials", Applied Materials Today, Vol 7, Pages 120–133, 2017.

[5] S. Ghosh and S. Lim, "A Miniaturized Bandpass Frequency-selective Surface Exploiting Three-Dimensional Printing Technique," in IEEE Antennas and Wireless Propagation Letters, vol. 18, no. 7, pp. 1322-1326, July 2019, doi: 10.1109/LAWP.2019.2915048.

[6] Ren LS, Jiao YC, Zhao JJ, et al. RCS reduction for a FSS-backed reflect array using a ring element. Prog. Electromagnet Res. Lett. 2011; 26:115– 123.

[7] Jun, S. and Sanz-Izquierdo, Benito and Parker, Edward A. (2016) 3D printing technique for the development of non-planar electromagnetic bandgap structures for antenna applications. Electronics Letters, 52 (3). pp. 175-176. ISSN 0013-5194.

[8] Sanz-Izquierdo, B. and Parker, E.A.: 'Frequency-selective Surfaces Formed by Partially Metalising 3D-printed Shapes', in, Antennas and Propagation (EuCAP), 2015 9th European Conference on, (2015).

[9] Sanz-Izquierdo, B. and Parker, E.A.: '3-D printing of Elements in Frequency-selective Arrays', IEEE Trans. Antennas Propag., 2014, 62, (12), pp. 6060-6066.

[10] Sievenpiper, D., Zhang, L.J., Broas, R.F.J., Alexopolous, N.G., and Yablonovitch, E.: 'High-Impedance Electromagnetic Surfaces with a Forbidden Frequency Band', IEEE Trans. Antennas Propag., 1999, 47, (11), pp. 2059-2074.

[11] Shaozhen, Z. and Langley, R.: 'Dual-Band Wearable Textile Antenna on an Ebg Substrate', IEEE Trans. Antennas Propag., 2009, 57, (4), pp.926-935.Kim, S., Yu-Jiun, R., Hoseon, L., Rida, A., Nikolaou, S., and Tentzeris, M.M.: 'Monopole Antenna with Inkjet-Printed Ebg Array on Paper Substrate for Wearable Applications', IEEE Antennas Wireless Propag. Lett, 2012, 11, pp. 663-666.

[12] Bin, L., Sanz-Izquierdo, B., Parker, E.A., and Batchelor, J.C.: 'A Frequency and Polarization Reconfigurable Circularly Polarized Antenna Using Active Ebg Structure for Satellite Navigation', IEEE Trans. Antennas Propag., 2015, 63, (1), pp. 33-40.

[13] Nicolson, A.M.; Ross, G.F. Measurement of the Intrinsic Properties of Materials by Time-Domain Techniques. IEEE Trans. Instrum. Meas. 1970, 19, 377–382.

[14] Weir, W.B. Automatic measurement of complex dielectric constant and permeability at microwave frequencies. Proc. IEEE 1974, 62, 33–36.

[15] Perspective on 3D Printing of Separation Membranes and Comparison to Related Unconventional Fabrication Techniques, Journal of Membrane Science; Published by Elsevier, 2017.

[16] Parulski, C.; Jennotte, O.; Lechanteur, A.; Evrard, B. Challenges of fused deposition modeling 3D printing in pharmaceutical applications: Where are we now? Adv. Drug Deliv. Rev. 2021, 175, 113810.

[17] Syrlybayev, D.; Zharylkassyn, B.; Seisekulova, A.; Akhmetov, M.; Perveen, A.; Talamona, D. Optimisation of strength properties of FDM printed parts—A critical review. Polymers 2021, 13, 1587.

[18] Rosli, A.A.; Shuib, R.K.; Ishak, K.M.K.; Hamid, Z.A.A.; Abdullah, M.K.; Rusli, A. Influence of bed temperature on warpage,shrinkage and density of various acrylonitrile butadiene styrene (ABS) parts from fused deposition modelling (FDM). AIP Conf. Proc. 2020, 2267, 1–10.

[19] Triyono, J.; Sukanto, H.; Saputra, R.M.; Smaradhana, D.F. The effect of nozzle hole diameter of 3D printing on porosity and tensile strength parts using polylactic acid material. Open Eng. 2020, 10, 762–768

[20] Wudy, K.; Lanzl, L.; Drummer, D. Selective laser sintering of filled polymer systems: Bulk properties and laser beam material interaction. Phys. Procedia 2016, 83, 991–1002.

[21] Melchels, F.P.W.; Feijen, J.; Grijpma, D.W. A review on stereolithography and its applications in biomedical engineering. Biomaterials 2010, 31, 6121–6130.

[22] Wu, W.; Ye, W.; Wu, Z.; Geng, P.; Wang, Y.; Zhao, J. Influence of layer thickness, raster angle, deformation temperature and recovery temperature on the shape-memory effect of 3D-printed polylactic acid samples. Materials 2017, 10, 970.

[23] J. W. Schultz, “Focused Beam Methods”, Measuring Microwave Materials in Free Space, (pp 46-52), 2012.

[24] Retrieved from https://www.mse.iastate.edu/files/2011/07/polymer-lab-instron-procedure.pdf, December 22, 2022.

[25] Reference image retrieved from www.admet.com ADMET, 2019, December 18, 2022.

[26] Retrieved from https://www.engineeringarchives.com/les_mom_offsetyield

method.html, December 18, 2022.

[27] Retrieved from https://www.robotistan.com/creality-gelistirilmis-ender-3-v2-3d-yazici, December 19, 2022.

[28] Retrieved from https://www.robotistan.com/anycubic-photon-s-3d-printer, January 1, 2023.

[29] Retrieved from https://www.stratasys.com/siteassets/3d-printers/printer-catalog/fdm-printers/f123-series-printers/wp_fdm_r--r-report_1021a.pdf?v=49ef81, January 1, 2023.

[30] Retrieved from https://markforged.com/3d-printers/x7, January 1, 2023.